Politecnico di Milano

Faculty of Systems Engineering

Bachelor thesis in Engineering Physics

Fiber Bragg Gratings for material characterization towards chiral gratings fabrication

Author:
Tommaso Stefano CARZANIGA
Matr. 728003

Supervisors:
Dr. M. Fokine [KTH]
Dr. S. Longhi [PoliMi]

Milano 2013

Abstract

In addition to the optical fibers themselves, telecommunications requires an in-fiber technology to manipulate light of different wavelengths within the fiber and to merge and separate light into or out of a fiber.
Wavelength selectivity can be achieved in fibers by imposing a periodic modulation of the refractive index along the fiber.
The high-precision knowledge of glass properties is essential towards drawing special fibers and all fiber based optical components manufactured by thermal processing like fiber tapers, couplers, long period gratings, chiral gratings [1] and micro-resonators [2]. Fundamental glass properties like viscosity, strain-optic coefficients, thermo-optic coefficients, thermal expansion coefficients change with temperature and we don't have yet an extensive and complete literature of data and methods which will enables us to improve our procedures.
This work starts with a preliminary experiment on fiber chiral gratings fabrication from a twin-hole optical fiber with the heat of a CO_2 laser beam. Microscope analysis suggest to further study the CO_2 laser beam temperature profile and thermo-mechanical properties of the fiber to avoid the collapse of the holes and breakage of the linearity of the fiber.
Thereupon we have successfully used Chemical Composition Gratings (CCGs), a special type of high-temperature stable in-fiber optical sensor, to characterize a CO_2-laser beam with high-resolution in space and temperatures, even exceeding the softening point of glass.
With a precise knowledge of the laser beam profile it was possible to further develop a modification of the fiber elongation method for viscosity characterization.
This modified method analyse the reflected Bragg wavelength evolution of a CCG heated by the CO_2-laser beam. We measure the evolution of the grating period so, instead of tens of cm's we analyse changes in length of half a μm with a resolution of $1pm$, and preliminary experiments demonstrated the effectiveness of CCGs in high-temperature characterization, their potential use for heat-capacity and effective viscosity measurements.

Keywords: Optical Fiber, Fiber Bragg Gratings, Chemical Composition Gratings, Chiral Fiber Gratings, Glass, Viscosity, Transition Temperature

Contents

List of Figures

Acknowledgements

I am grateful to Micheal Fokine, who taught me the importance of a meticulous methodology and organization before the start of the practical part of an experiment, who gave me the incredible chance to visit Brazil and there present our work. His quenchless curiosity and his advices about my future mean a lot to me.
To Patrick Holmberg for his valuable help, for being a guide in the lab and for having endured and wisely answered all my questions.
To Stefano Bonetti, for having told me about the quality of the Laser Fysik group of Fredrik Laurell.
To Fredrik Laurell, for having welcomed me in his prestigious group.
To Jens Aage Tellefsen and Lars-Gunnar Andersson, for their warm welcome and the administrative help they gave me anytime I needed it.
To Katia Gallo, who incited me to continuously research.
To the Laser Fysik group, for the fika every Friday afternoon and the incredible atmosphere in the group.
To Claudia Dallera, for having tutored me in the T.I.M.E. project.
To Philippe Pernod and Stefano Longhi, for having tutored me respectively from the École Centrale de Lille and from the Politecnico di Milano.
To Eleftherios Karachalias, Marco Tito Bordogna and many others, for the fellowship through the lectures of the Swedish course at KTH and the nights spent together during the European Football Championship.

Chapter 1

Introductory concepts

In order to understand the theoretical background on which the experiments and results presented in this thesis are based on, I will discuss a few basic concepts the reader may not be familiar with.

1.1 What is glass?

Glasses still have mysterious aspects [7]. It is not easy to state a simple definition which explains all the main features of this intriguing material.
The American Society of Testing Materials (ASTM) define glass as:

> " inorganic product of fusion (...) cooled to a rigid condition without crystallizing".

This definition is limited and even wrong in a few aspects. We now know many organic glass systems, so glasses are no longer just inorganic. We now know glasses made by sol-gel processes or chemical vapour deposition, so glasses are no more just a product of fusion.
The key idea which arises from this definition is the undoubted duality glass-crystal.
Compared to a crystal, a glass do not have a well-defined melting point [8].

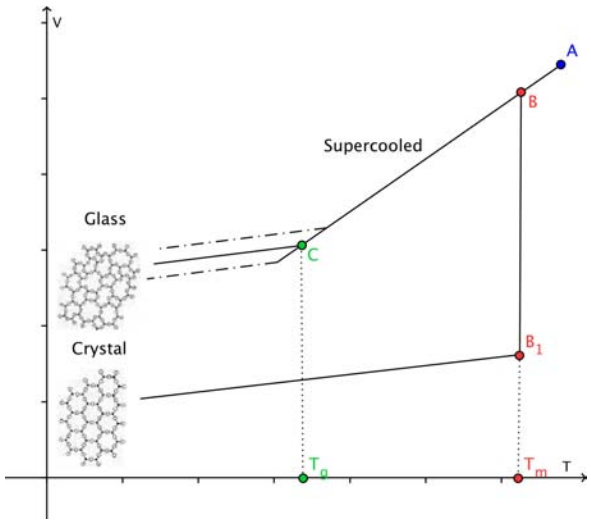

Figure 1.1: Schematic VT diagram and illustration of the atomic arrangement in crystals and glasses.

Imagine the material is at high temperature (point A in Fig. 1.1). We start cooling the material. If the cooling rate is high enough, the nucleation can be avoided and the crystallization does not

occur (point B). The **viscosity**[1] of the system rapidly increases and the molecular groups can not rearrange themselves fast enough to reach the volume characteristic of that temperature. The **relaxation times** increase drastically. If we continue to cool we will reach the temperature at which the VT curve behaves as a solid. We have reached the glassy state.
The onset of the transition from a liquid to a glass is established at the temperature T_g, where relaxations times are about 100 seconds and the viscosity reaches the value of $10^{12} Pa \cdot s$.
In contrast to crystallization, the glass transition is not a first-order phase transition in the Ehrensfest classification. Therefore, the glass transition temperature is not fixed and weakly depends on the cooling rate. The glass transition implies discontinuities in properties like volume, energy and viscosity.
There are different methods to measure the glass transition temperature of a material:

- Differential scanning calorimetry (DSC)
- Thermomechanical analysis (TMA)
- Dynamic mechanical analysis (DMA)

In the works presented in the thesis we propose a calorimetric method to obtain the value of the glass transition temperature.
In glasses, as in many other materials, physical properties depends both on instantaneous temperature and thermal history [9]. As the temperature varies, we got vibrational and structural changes (the latter of these occur much more slowly than the former) [10].
In a complicated material like glass there are many structural changes that can be identified with the breaking and reformation of various atomic bonds, and occur over a wide range of temperatures and time-scales.
Due to their temperature-dependent viscosity, glasses behave like Newtonian liquids at high temperatures and structural changes are completed immediately. If we go to low temperatures the structure is frozen and the glasses behave like a linear thermoelastic solid. But it is at intermediate temperatures, when glass is mechanically visco-elastic, that the time needed for structural changes has about the same order of magnitude as the time-scales of glass processing. We then need to know both the instantaneous temperature and thermal history to characterize the material.
The scalar fictive temperature is the temperature at which a material property is at equilibrium [11]. This concept was introduced by Tool in 1946 [12] [13] [14].

1.2 What is an optical fiber?

Now we know what is glass, but why is it so important for telecommunication?

> " Optical fibers have revolutionized telecommunication. Much of the success of optical fiber lies in its near-ideal properties: low transmission loss, high optical damage threshold, and low optical non-linearity. The combination of these properties has enabled long-distance communication to become a reality " [15].

Thanks to great advances in silica processing, losses for optical fibers are only $0.2 dB \cdot Km^{-1}$. Losses are so low because of many advantageous material properties. Fused silica has a bandgap of $\sim 9eV$, which corresponds to 0.138 μm, while the infrared vibrational resonances produce an edge at a wavelength of around $2\mu m$. Absorption is so at higher energies compared with vibrational excitation. Fused silica can be produced with an almost perfect homogeneity, making Rayleigh scattering the dominant loss mechanism with its characteristic λ^{-4} [16].
Light is then able to travel tens of kilometers in the 1550 nm region (third telecommunication window).
The main structure of an optical fiber is simple, as can be seen in Fig. 1.2. The doped core region has a higher refractive index than the surrounding material (cladding), which is usually made of silica. Light is trapped in the core by total internal reflection (Eq. 1.1) at the core-cladding interface.

[1] We will discuss in more detail the concept of viscosity in Chapter 4.

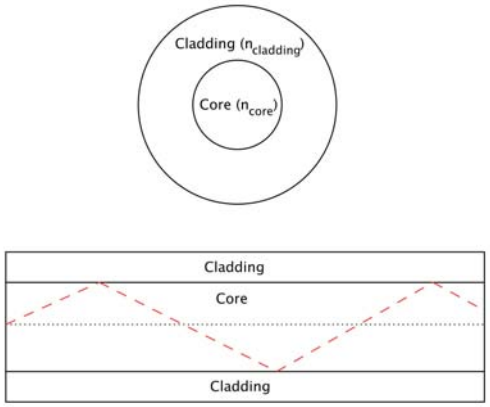

Figure 1.2: Schematic illustration of the basic concepts of how an optical fiber works.

$$\sin\theta_i = \frac{n_{cladding}}{n_{core}} \tag{1.1}$$

The most commonly used core dopant, which was used also in this thesis, is germanium. It belongs to Group IVA, as does silicon, and replaces the silicon atom within the tetrahedron, coordinated with four oxygen atoms.
For step-index fibers we can distinguish single-mode and multi-mode behaviour by the use of a dimensionless parameter, referred to as the normalized frequency

$$V = \frac{2\pi a}{\lambda}(n_1^2 - n_2^2)^{1/2} \tag{1.2}$$

The electromagnetic theory of propagation states that a fiber is single-mode when $V < 2.4048$ [17].

1.3 What is a fiber Bragg grating?

When we have made an optical fiber from glass we can go even further and treat the light while it run through the fiber.

1.3.1 History of FBGs

At the Canadian Communication Research Center in 1978 Ken Hill et al. discovered the photosensitivity of optical fibers by using germania-doped silica fiber on an experiment with visible argon ion laser radiation [18].
Light launched into fibers was increasingly reflected, as a function of time, thanks to a refractive index grating written in the core of optical fibers, created by a standing wave intensity pattern which was the result of the back reflection of the far end of fibers and forward-propagating light. The increase in reflection made the refractive index grating grow, besides increasing standing wave pattern intensity.
In 1989 Gerry Meltz et al. found the way to free the process from the constraint of the incident beam wavelength [19]. With holographic writing using single-photon absorption at 244 nm a grating is made thanks to the interference pattern of two beams. It was then possible to shift the Bragg condition to more useful wavelength, dependent on the interference angle, like the third telecommunication window.
The last breakthrough was made by Lemaire et al. who discovered that hydrogen loaded standard fibers can be written with large refractive index modulation [20].

1.3.2 Principles of FBGs

Fiber gratings are essential elements for controlling light in photonics, telecommunications and sensing.

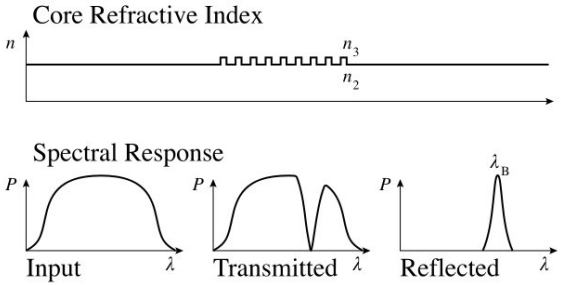

Image released under GFDL licence.

A fiber Bragg grating is a periodic or aperiodic perturbation of the effective refractive index in the core of an optical fiber.
The perturbation is approximately periodic over a certain length (few millimeters or centimeters), and the period is in the order of hundreds of nanometers or much longer, depending on the type of grating involved [21].
The refractive index perturbation leads to the reflection of light propagating along the fiber in a narrow range of wavelengths, for which a Bragg condition is satisfied

$$\frac{2\pi}{\Lambda} = 2 \cdot \frac{2\pi n_{eff}}{\lambda} \tag{1.3}$$

which leads to

$$\lambda = 2n_{eff}\Lambda \tag{1.4}$$

where Λ is the grating period, λ is the vacuum wavelength, and n_{eff} is the effective refractive index of light in the fiber.
For a single-mode ($0 < V < 2.4048$) step-index fiber, the normalized propagation constant is

$$b = \frac{\beta^2 - k^2 n_2^2}{k^2 n_1^2 - k^2 n_2^2} = \frac{n_{eff}^2 - n_2^2}{n_1^2 - n_2^2} [22] \tag{1.5}$$

It has been approximated as $b(V) = (A - B/V)^2$ and solved as $(1.1428 - 0.996/V)^2$ [22].
Therefore the effective refractive index is

$$n_{eff} = \sqrt{b \cdot NA^2 + n_{cl}^2} \tag{1.6}$$

A convenient approximation for the effective refractive index is then

$$n_{eff} \approx n_{cl} + (1.1428 - 0.996/V)^2 \Delta n \tag{1.7}$$

where V is the $V - value$ of the fiber, and Δn is the core-cladding refractive index difference.
Essentially, Eq. 1.4 means that the wavenumber of the grating matches the difference of the opposite wave vectors of the incident and reflected waves. In that case, the complex amplitudes corresponding to reflected field contributions from different parts of the grating are all **in phase** so that they can add up constructively.
Even a weak index modulation (10^{-4}) is sufficient for achieving nearly total reflection, if the grating is a few millimeters long.
The spectral reflectivity of the grating, solved using coupled-mode theory, is given by

$$R(L, \lambda) = \tanh^2 \left(\frac{\pi \Delta n L}{\lambda} \eta \right) [23], \tag{1.8}$$

where L is the grating length, λ is the reflected wavelength and η is the overlap between the fundamental mode and core.
Typical values of η are $\eta = 0.8 - 0.9$. The spectral FWHM of the grating is given by

$$\Delta\lambda = \lambda_B \cdot s \cdot \sqrt{\left(\frac{\Delta n}{2n_0}\right)^2 \left(\frac{1}{n}\right)^2} \tag{1.9}$$

where N is the number of fringes (typically $N \sim 20000$ for a 10mm long grating) and the pre-factor s is $s \sim 0.5$ for weak gratings and $s \sim 1$ for strong gratings.
We can control the refractive index modulation and the average refractive index along the grating so to decide the spectral properties of the grating in order to achieve the desired properties.
There is not just a single type of fiber Bragg Gratings (FBGs).
There are **short period gratings** with a typical period of $0.25 - 0.5\mu m$ (the light is coupled into the backward propagating direction). There are also long-period gratings with a typical period of $100 - 500\mu m$ (the light is coupled into forward propagating cladding modes).
These gratings can be fabricated by different processes. Type 0 gratings are the one discovered by Hill et al. [18]. Type I are characterized by monotonous growth. Type II are referred to as damage gratings because they are made by single-pulse radiation. A more detailed explanation can be found in [23].
Chemical composition gratings (CCGs) have optical properties not so different from type I gratings, although the manufacturing procedure, growth of refractive index and thermal properties are radically different. The refractive index modulation is due to a periodic variation of one or several dopants in the core. The decay mechanism of chemical composition gratings requires diffusion of the modulated dopants. This process is what gives these gratings exceptional thermal stability [24]. Thermal stability is the property we will base on most of the experiments showed in this thesis.
This was just a basic introduction to understand the main points of the work carried out in this thesis. To have a more complete and deeper description of the physics involved in fiber Bragg gratings I strongly recommend the book of Raman Kashyap [25].
A major part of the work I carried out during the internship was to gain the required *savoir faire* to deal with short period FBGs and mostly CCGs fabrication.

FBG fabrication

Therefore, I will briefly explain short period FBG fabrication (Fig. 1.3).
The phase mask diffract an incident UV beam into several orders, $m = 0, \pm1, \pm2, \cdots$.
The incident and diffracted orders satisfy the general diffraction equation, with the period Λ_{pm} of the phase-mask,

$$\Lambda_{pm} = \frac{m\lambda_{uv}}{\left(\sin\frac{\theta_m}{2} - \sin\theta_i\right)} [26] \tag{1.10}$$

where $\theta_m/2$ is the angle of the diffracted order, λ_{uv} the wavelength, and θ_i the angle of the incident UV beam.
With the UV radiation at normal incidence, $\theta_i = 0$, the diffracted radiation is split into $m = 0$ and ±1 orders.
The beam at $m = 0$ is blocked. The interference pattern at the fiber of the two beams of orders ±1 brought together by parallel mirrors has a period Λ_g related to the diffraction angle $\theta_m/2$ by

$$\Lambda_g = \frac{\lambda_{uv}}{2\sin(\theta_m/2)} = \frac{\Lambda_{pm}}{2} \tag{1.11}$$

CCG fabrication

The CCGs used in this study were manufactured in $F - GeO_2$ doped silica fibers [24]. I will briefly explain the fabrication process.
The fiber is hydrogen loaded at 10MPa and 323K for 5 days before grating inscription.
We then write the FBG by use of standard side-writing techniques.

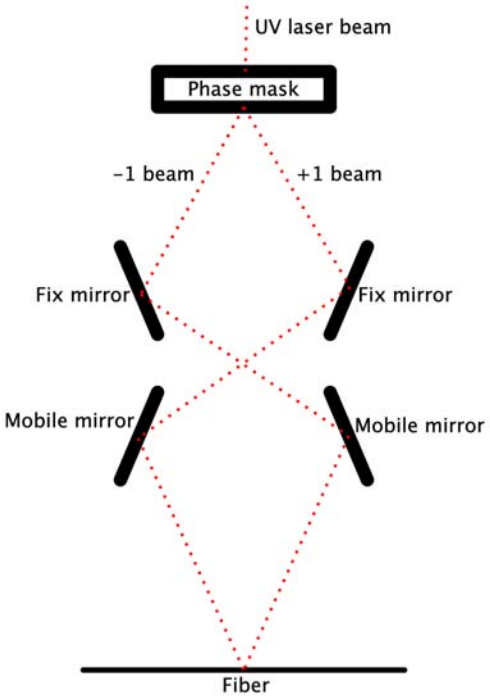

Figure 1.3: Scheme of the setup for FBG fabrication.

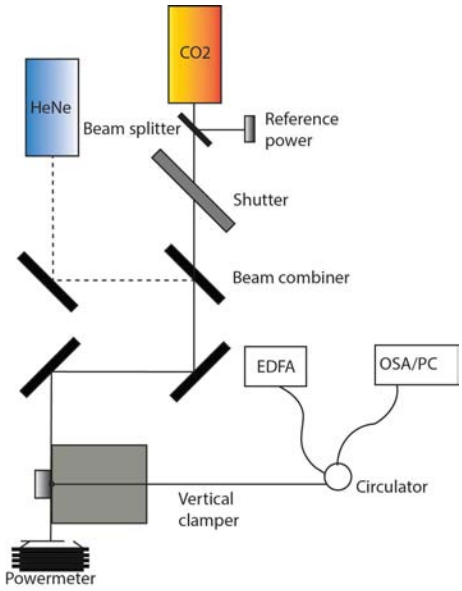

Figure 1.4: Scheme of the experimental setup for CCGs fabrication.

The experimental setup to develop an FBG into a CCG is explained in Fig. 1.4 and Fig. 1.5. The physical mechanisms involved in the process is still under studies. I will cite the most complete interpretation.

- Firstly we pre-anneal the FBG at $\sim 400K$ for 10 hours. During this step the H_2 is eliminated through diffusion.
- Then we anneal the grating at $\sim 900K$ for 90 minutes. This step probably involve reaction and diffusion mechanisms.

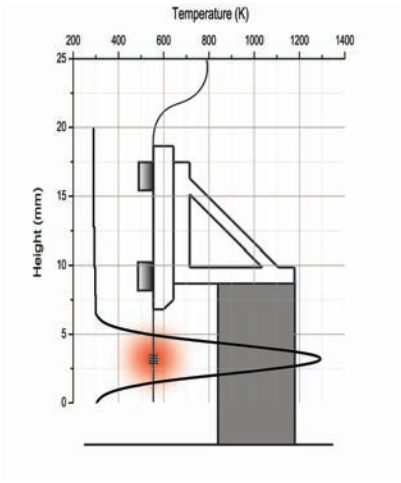

Figure 1.5: Vertical positioning of the fiber during the annealing and developing part.

- Finally we develop the grating at $\sim 1273K$ for 60 minutes. It is believed to cause structural relaxation which leads the modified glass structure towards equilibrium.

A recent kind of fiber grating

Chiral fiber gratings (CFGs) have similar optical properties as others FBG but radically differ in the manufacturing procedure. The refractive index is commonly modulated by twisting a fiber with noncircular core cross section as it is pass through a miniature oven. Short period chiral gratings ($\sim 1\mu m$) can be used as filters and lasers. Intermediate period chiral gratings ($\sim 10\mu m$) can be used as polarisers, whereas long period chiral gratings ($\sim 100\mu m$) can be used as sensors [27].
The initial aim of the internship was to control the fabrication of a non-classical CFG, based on a twin-hole optical fiber processed by the heat of a CO_2 laser beam (Chapter 2).
Nevertheless, to better control the process we needed to characterize as much as possible material properties and the optical system. After having characterized the temperature profile of the $CO_2 beam$ (Chapter 3) we focused our attention on the viscosity characterization of the fiber (Chapter 4) and we developed a new method to characterize optical fiber viscosity.

Chapter 2

Fabrication of chiral fiber gratings (CFG)

The aim of this first experiment is simply to try to develop chiral gratings in silica optical fiber. Without having done any specific investigation we have tried to discover and analyse the key factors underlying the process of chiral gratings fabrication.

2.1 Experimental setup

To fabricate a helicoidal fiber grating we twisted twin-hole silica fibers under a continuous single-side CO_2 laser beam exposure.

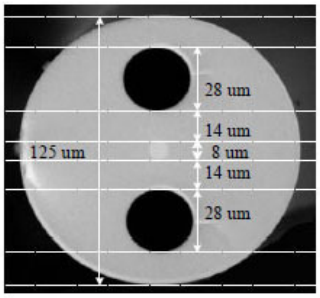

Figure 2.1: Profile of the twin-hole fibre from Acreo used in this work.

At high temperature (above T_g) the fiber softens and is slowly deformed under the torque applied. So it becomes possible to induce large and fast twists, which would destroy the fiber at room temperature. In our case the core-cladding eccentricity usually responsible for this kind of grating structure is substitute by the twin-hole inside the cladding, which rotates around the core.
Each fiber cross section with a longitudinal coordinate x is rotated by an angle $\phi = 2\pi x/\Lambda$, where Λ is the period of the helicoid and is related to the number of turns N. The length of the twisted fiber section L by the following relationship $\Lambda = L/N$.
The experimental set-up is shown in Fig. 2.2.
The laser used to heat the fiber is a CO_2-laser ULR-25 with a maximum output power of 28 W and a $1/e^2$-diameter of $\sim 6.5mm$. The CO_2 laser produces a beam of infra-red light with the principal wavelength band centred around $10.6\mu m$. We used a carbon dioxide lasers for two main reasons. Firstly the absorption coefficient of fused silica has one of its highest value at $10.6\mu m$ (Fig. 2.3). Then, this kind of laser is one of the the highest-power continuous wave laser that is currently available.
Because CO_2 lasers operates in the infra-red, we needed optical components made of special materials. The mirrors were silvered, while windows and lenses were made of Zinc-Selenide.
We can control and regulate the output power of the CO_2 laser. Patrik Holmberg, a member of the Laser Fysik group, has obtained the power of the beam at the fiber, after having been modified by

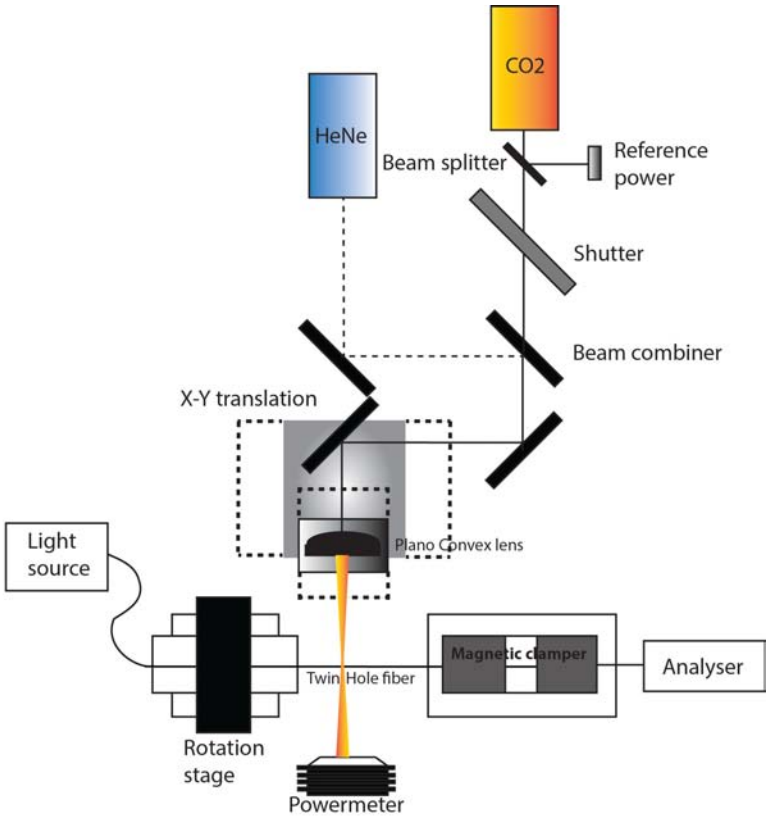

Figure 2.2: Extensive scheme of the chiral gratings experimental set-up

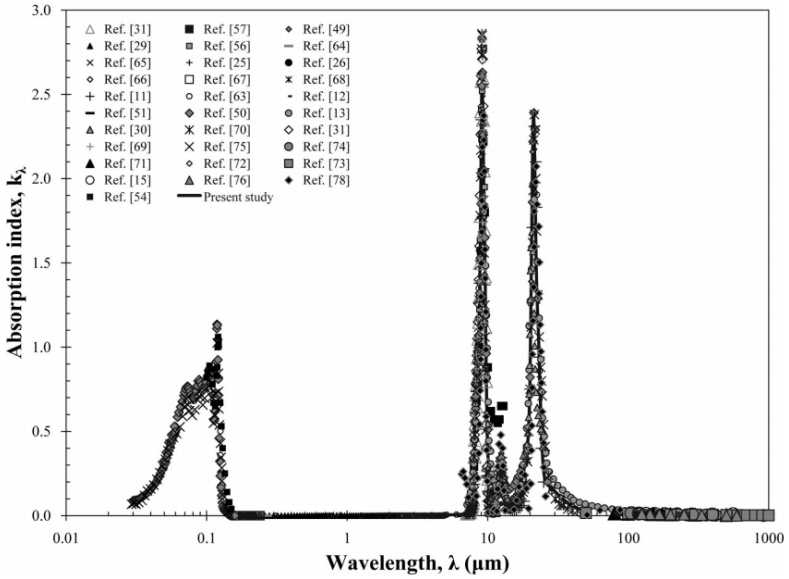

Figure 2.3: IR absorption spectra of fused silica [3].

the optical components, against the PWM modulation. By means of an FBG sensing experiment, he also obtained the temperature of silica fiber at different beam intensity. The rise time of the temperature in the fiber due to CO_2 laser heating is almost independent from the power and is $\sim 0.42s$.
The experimental set-up is theoretically simple but practically there are a couple of obstacles which are not easy to overcome.

2.1.1 Alignment of the rotation stage

To make the fiber straight we needed a perfect alignment of the rotation stage (Fig. 2.4). Apply a longitudinal load is not the best choice as you stretch irreversibly the fiber when you heat it.

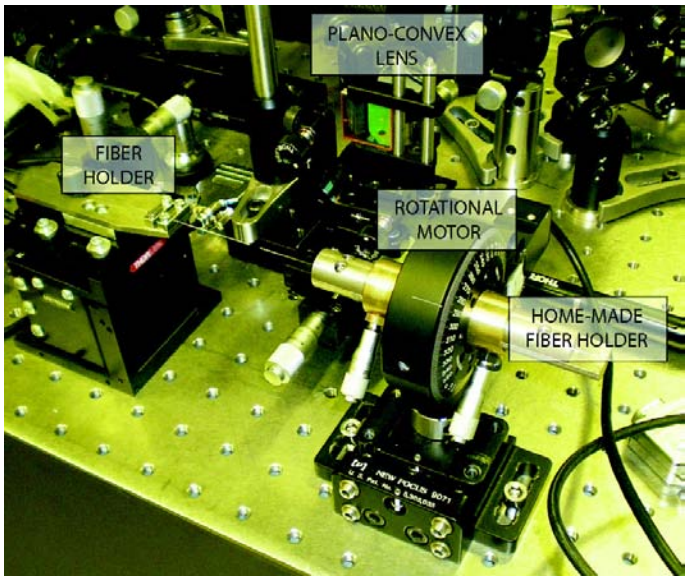

Figure 2.4: Photo of the chiral gratings experimental setup

To build up the rotation stage we used a PRM1/MZ8 motorized precision rotation stage from Thorlabs combined with an home-made fiber holder realized by Patrik Holmberg, a PhD student from the Laser Fysik department.
To align this device we needed to control four screws so to create a perfect axis of rotation. We used two cameras, a CCD (DCU223M from Thorlabs) and a CMOS (DCC1545M again from Thorlabs) with 20X objectives to get a high resolution alignment on a laboratory bench, Fig. 2.5. To control the rotation of this stage I wrote a simple program in VB (Appendix A).

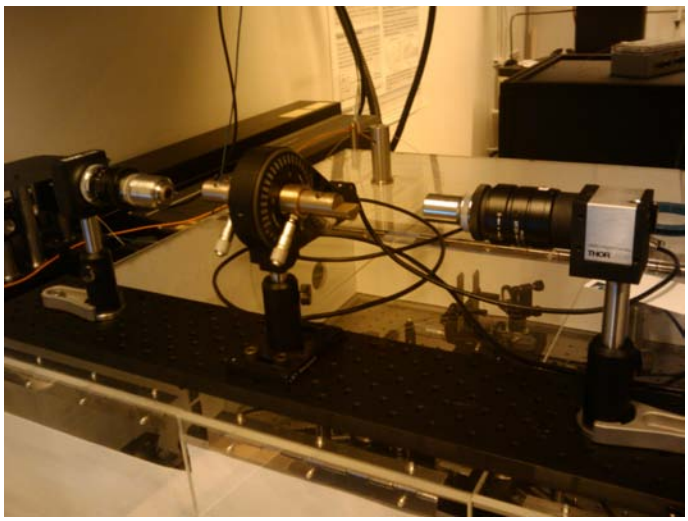

Figure 2.5: Alignment setup for the rotation stage

Thanks to a HeNe laser injected in the optical fiber, we could ameliorate the alignment of the rotation stage (Fig. 2.6). Although the process was difficult and time consuming, it led to a high precision calibration.

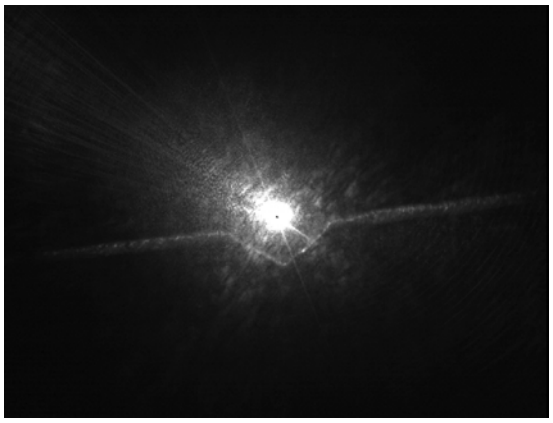

Figure 2.6: Alignment visual method for the rotation stage.

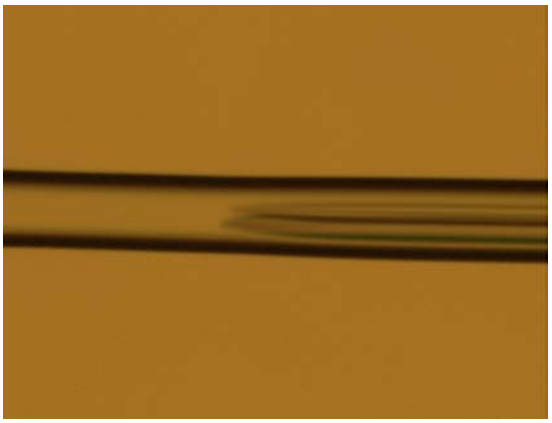

Figure 2.7: Image of the splicing region between a Twin-Hole Fiber and a SMF-28

2.2 Results

2.2.1 Quantized twists

The first experiment we did was to measure the losses in the light transmitted through the fiber at each twist.
We spliced [1] the twin-hole fiber to a SMF-28 fiber and we measured losses for rapid twists of the fiber using a white light source and an analyser, as show in Fig. 2.2.
The twists were performed rapidly. We rotated the motor 180 degrees at room temperature and then we sent a CO_2 laser pulse of $0.3s$ with an intensity of about $1.4W/mm^2$ directly to the fiber.

Figure 2.8: Optical losses after mechanical twists of the fiber.

No major losses were measured (Fig. 2.8), just a transition due probably to polarization effects. We assumed that the difference between the two figures is due to the fact that the twists were done with different handiness.

2.2.2 Continuous twists

The second experiment was to continuously twist the fiber with a rotation speed of 20 $^\circ/s$ and heat it with a CO_2-laser Gaussian beam. Without using the focusing plano-convex lens (unlike shown in Fig. 2.2) the beam had a $1/e^2$ diameter of $\sim 6.5mm$ and an intensity of about $1.3W/mm^2$.
Analysing the data we could plot the evolution of the distribution of the twists on the surface of the fiber and their widths (Fig. 2.9).
We also analysed the evolution in time of the heated region, which for us was the total twisted region, and of the width of the central twist (Fig. 2.10).

[1] The splicing process between optical fibers which differs in geometry and composition (Fig. 2.7) is a complex topic and herein I will not go deeper in covering this aspects.

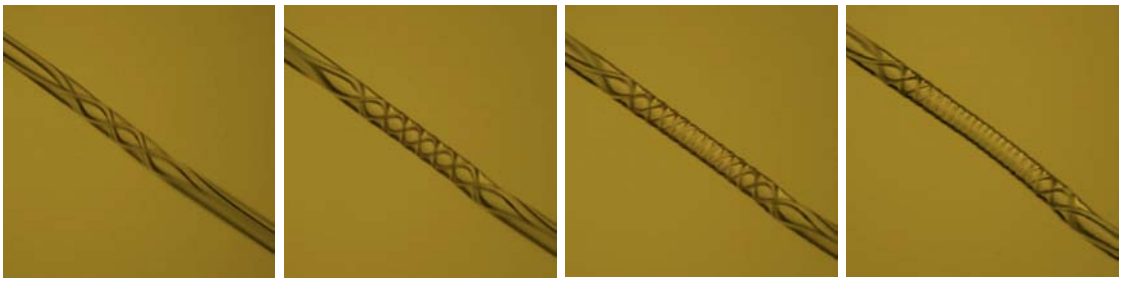

Fiber twisted for 54s | Fiber twisted for 145s | Fiber twisted for 313s | Fiber twisted for 448s

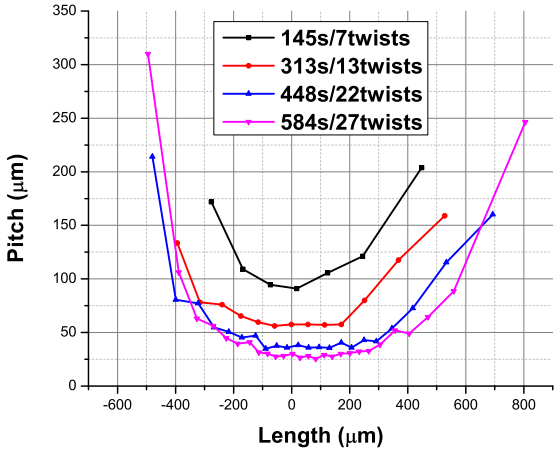

Figure 2.9: Evolution of the width of every twist in time.

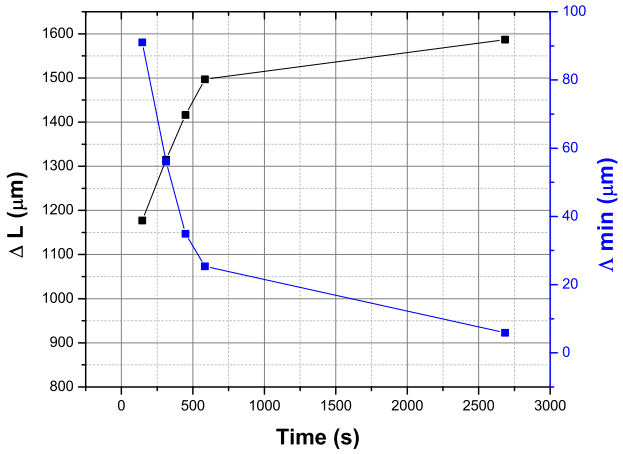

Figure 2.10: Evolution of the minimum pitch of a twist in time.

From these graphs and curves we can make predictions on what would be the evolution of the process if we keep twisting the fiber for more time.

2.2.3 Microscope analysis

Surface analysis

We analysed the surface status of the fiber at the microscope, which gave us a resolution of $1\mu m$.

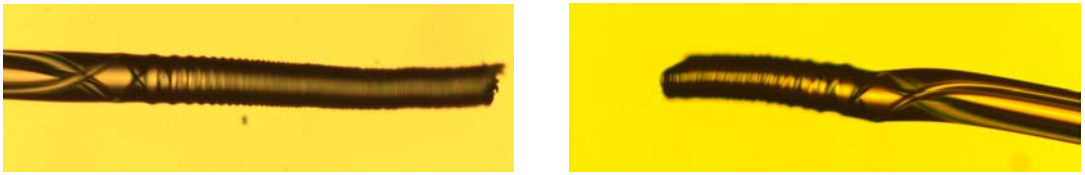

Figure 2.11: Optical twisted fiber broken by thermal shock.

If we look at the microscope image in Fig. 2.12 we can clearly count the number of twists.

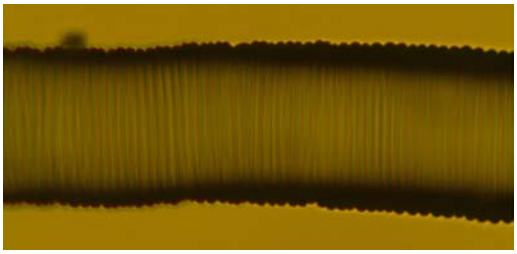

Figure 2.12: Rough profile of the fiber.

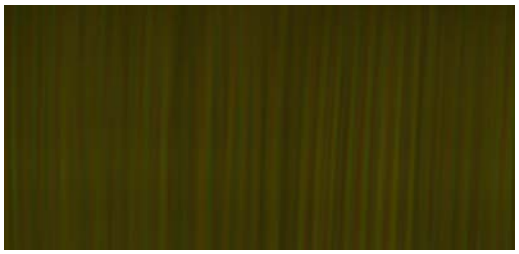

Figure 2.13: Optical fiber surface at 100x.

Despite the usefulness of the information collected from a surface analysis it was necessary to perform a deeper research on the status of the twin holes along the twisted fiber.

Polishing the fiber

We then decided to polish the fiber and analyse directly the evolution of the holes. I will briefly discuss the polishing procedure. In order to minimize the damages due to the polishing process we put our fiber in the middle of a microscope slice surrounded by parallel SMF-28 fibers, each one separated by a few millimetres, as shown in Fig. 2.14.

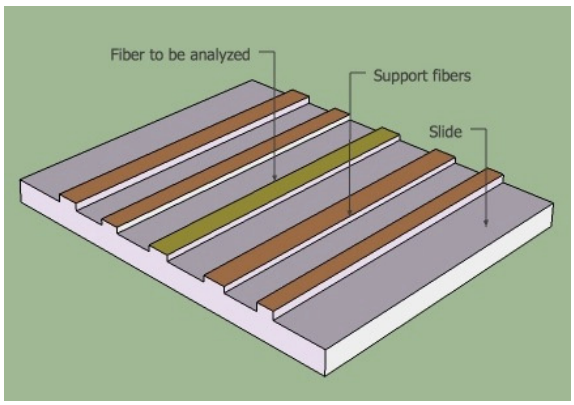

Figure 2.14: Slide preparation scheme for polishing the fiber.

We needed to fix the fibers to the slide. After having sprinkled the slide with some wax dust, we put the slide on a electric heater at $\sim 400K$ and we wait till the wax melts. We shut down the heater and we waited till the wax fix the fibers to the slide. We then worked with a polishing paper $1\mu m$ thick for a couple of minutes until the fiber was almost halved.

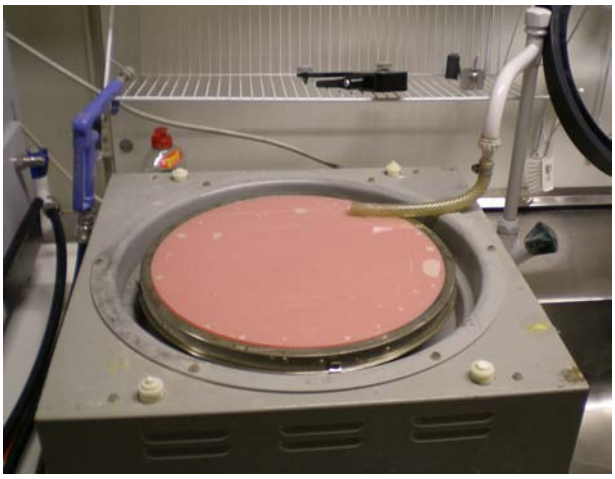

Figure 2.15: Polishing machine.

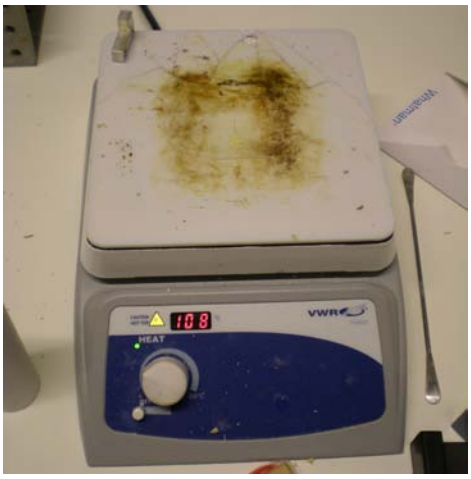

Figure 2.16: Laboratory heater.

Analysis of the polished fiber

We then performed the analysis of the polished fiber at the microscope.

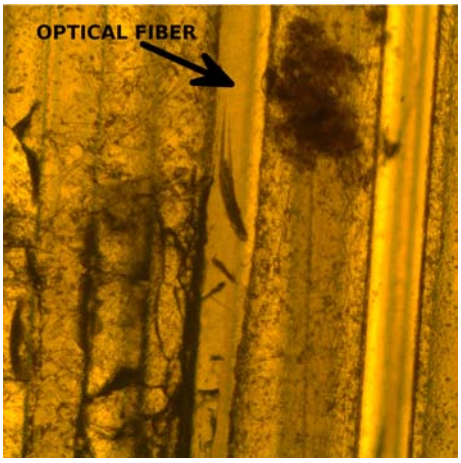

Figure 2.17: Microscope image at 5x.

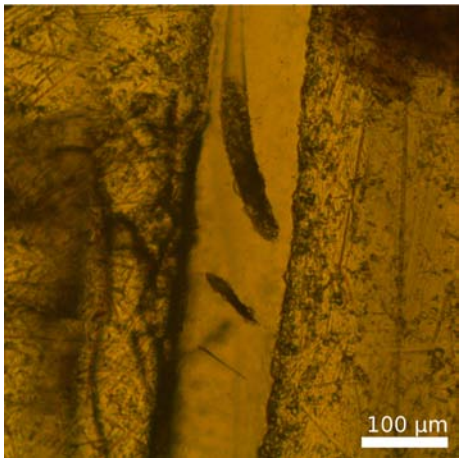

Figure 2.18: Microscope image at 10x.

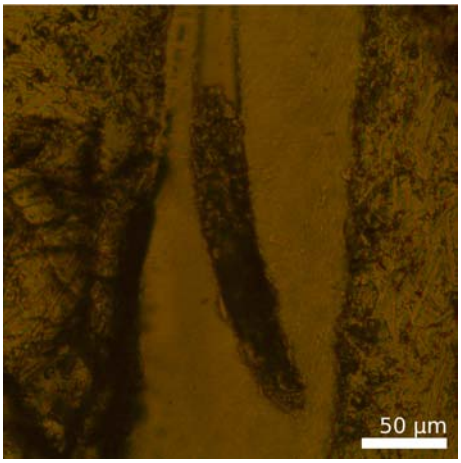

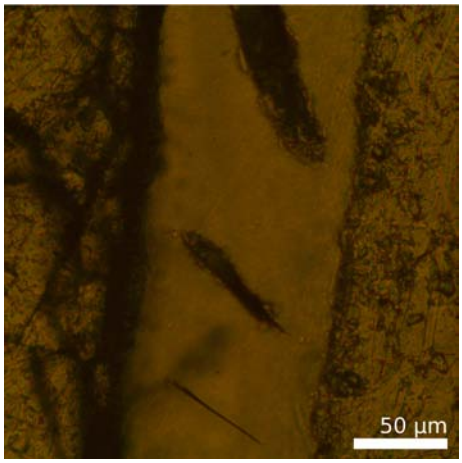

Figure 2.19: Images at microscope with 20x magnification.

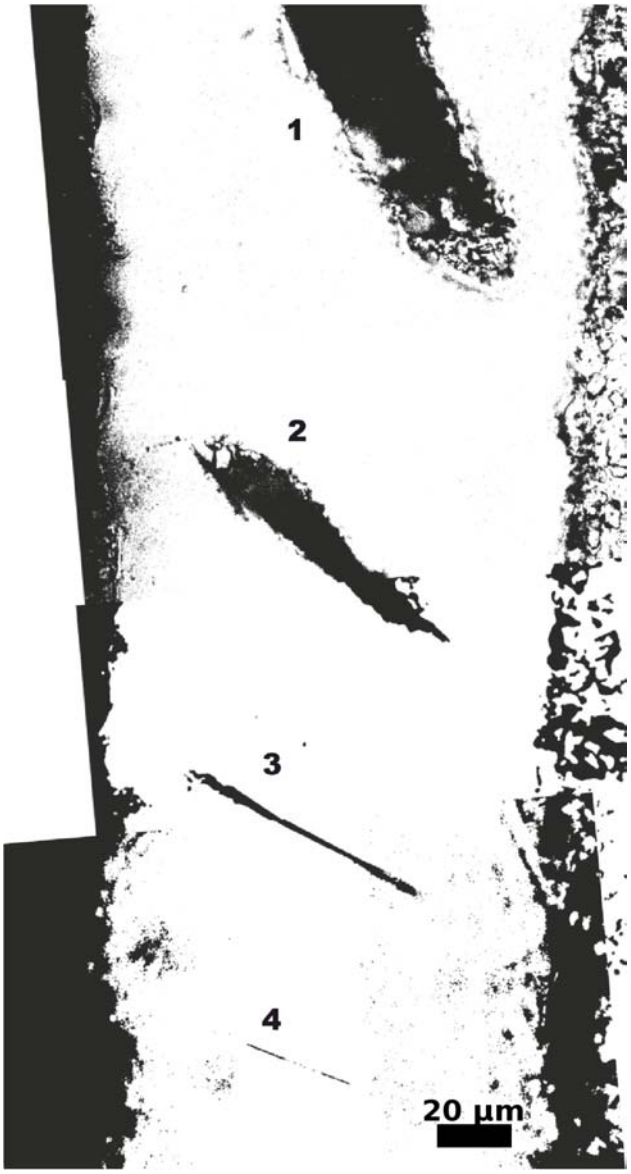

Figure 2.20: Image at microscope with 50x magnification after image treatment.

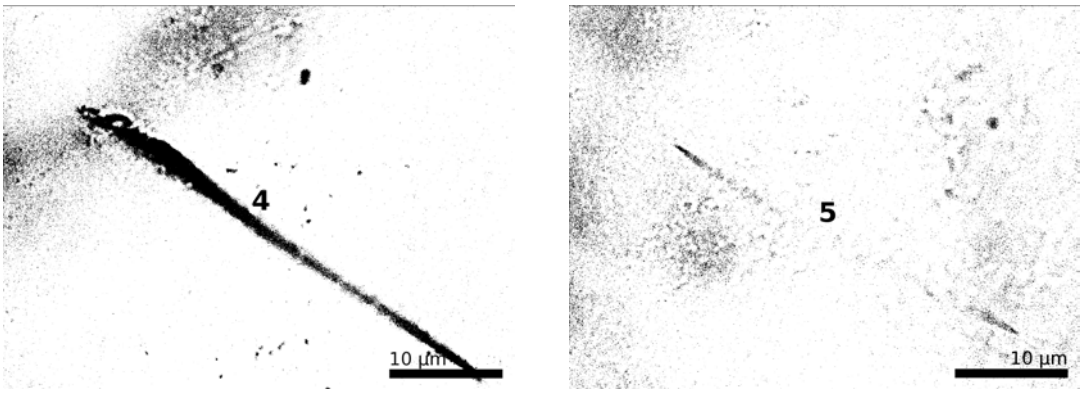

Figure 2.21: Images at microscope with 100x magnification after a threshold image treatment.

2.3 Discussion

Before the experiment the holes had a diameter of $28\mu m$. We then assume, from surface analysis, that the twisting region is around $1600\mu m$.
At first we made an approximation: we ignored the effects of surface tension and their impact on the holes development.
At every twist the length of the holes increase by $2\pi r$, which in our case is $200\mu m$.
Assuming that $V = \pi \cdot r^2 \cdot L = const$, we can obtain the average final radius of the holes

$$r_f = r_i \sqrt{\frac{L_i}{L_f}} \tag{2.1}$$

Entering our data we obtain $r_f = 14\sqrt{\frac{8}{8+n}}$, where n is the number of twists.

n	$r_f[\mu m]$
8	9.9
16	8.1
32	6.26
128	3.4

Analysing the information given by Fig. 2.20, which was treated with *de-noising*, *threshold* and *dust and scratch*, we noticed that the diameter of the holes goes down faster than we expected from the surface characterization and the first theoretical analysis.
Our prediction based on the surface of the fiber was incorrect. The reason is that we did not take into account the influence of surface tension and viscosity in the dynamical evolution of the holes at high temperature under torque.
The collapse of the holes is a big issue that could allow wide developments but that could also become a difficult obstacle to overcome if we want to maintain the twin-holes structure in the chiral grating.
To solve the problem of collapsing holes and distortion of the fiber profile we need to improve process control and for doing that we need to **characterize** the **temperature** of the laser beam $T(x, y)$ (consequently the beam profile and the heat capacity) and the **viscosity** $\eta(T)$.
We can do that thanks to FBGs sensors and we are going to explain it in the next two chapters.

Chapter 3

Temperature characterization

Before going through the analysis of the temperature characterization is necessary to understand how FBGs can be used as sensors and which are their characteristics.

3.1 Sensing properties of FBGs

The basic equation on which FBGs are based is

$$\lambda_B = 2n_{eff}\Lambda \tag{3.1}$$

Fiber gratings are used to sense a wide range of parameters, including temperature and strain.

Thermo-optic effect

There are two predominant causes for the change in the Bragg wavelength described by the thermo-optic coefficient, ξ:

- the change in the refractive index of the optical fiber
- the change in the physical length of the fiber through thermal expansion.

The evolution of the Bragg wavelength can be described as

$$\Delta\lambda_B = \lambda_B \left(\frac{1}{n_{eff}} \frac{dn_{eff}}{dT} + \alpha_T \right) \Delta T \tag{3.2}$$

or, in a more compact manner, as

$$\Delta\lambda_B = \lambda_B \left(\xi + \alpha_T \right) \Delta T \tag{3.3}$$

The real part of the refractive index can be written as a function of temperature (from 0°C to 700°C) as

$$n = 1.4646 + 2.37 \cdot 10^{-5} \cdot T - 2.7 \cdot 10^{-8} \cdot T^2 + 2.1 \cdot 10^{-11} \cdot T^3 [28] \tag{3.4}$$

and the thermal optical coefficient as a function of temperature can be expressed as follows

$$\frac{\partial n}{\partial T} = 2.37 \cdot 10^{-5} - 5.4 \cdot 10^{-8} \cdot T + 6.3 \cdot 10^{-11} \cdot T^2 \tag{3.5}$$

The average thermal optical coefficient is $6 - 8 \cdot 10^{-6} K^{-1}$.
The coefficient of thermal expansion α_T for fused silica is 5.5×10^{-7}[29].
The length change associated with temperature in silica contributes to only around 10% of the overall change in the reflected Bragg wavelength and is therefore dominated by the refractive index change.
The typical wavelength shift due to the temperature at a wavelength of $1550nm$ for a standard SMF-28 is $\Delta\lambda_B = 13.6pm/K$.

Photo-elastic effect

The dielectric constant of a material can be strain dependent. So, when this material is mechanically loaded, the photoelastic effect occurs and a birefringence is created. Under uniaxial tension or compression, an isotropic solid takes on the properties of a uniaxial crystal with the optical axis parallel to the axis of tension or compression [30].
It is the deformation of the electron shells of atoms and molecules and the consequent orientation of optically anisotropic molecules or components of such molecules to cause the photoelastic effect. The birefringence cause a relative phase difference between the two components of an electromagnetic wave propagating in the material or between the same component propagating in a loaded or unloaded material (for example an optical fiber), described as

$$\Delta = \frac{2\pi l}{\lambda}\rho_\alpha(\Delta\sigma)[31] \tag{3.6}$$

where Δ is the phase difference, l is the length of the specimen, C is the stress-optic coefficient and $\Delta\sigma$ is the difference between the two stresses.
The Bragg wavelength shift as a function of the physical elongation and the Pockels coefficients is described by

$$\Delta\lambda_B = \lambda_B(1-\rho_\alpha)\epsilon \tag{3.7}$$

where ρ_α, the stress-optic coefficient, is

$$\rho_\alpha = \frac{n_{eff}^2}{2}[\rho_{12} - \nu(\rho_{11}-\rho_{12})] \tag{3.8}$$

where ν is the Poisson's ratio, λ_B and $\Delta\lambda_B$ are the Bragg wavelength and wavelength shift respectively, P is an effective strain-optic term and ρ_{11}, ρ_{12} and ρ_{44} are the strain tensor components related to axial loading where $\rho_{12} = \rho_{11} - 2\cdot\rho_{44}$ due to the cylindrical symmetry of the system. Literature values for ρ_{11} and ρ_{44} are 0.113 and -0.069 respectively, so ρ_{12} is 0.251.
The typical wavelength shift due to the strain at a wavelength of $1550nm$ for a standard SMF-28 is $\Delta\lambda_B = 1.209pm/\mu\varepsilon$.

Temperature and strain sensing

The complete equation which describes the shift of a Bragg wavelength of a CCG due to strain and temperature can be expressed as

$$\Delta\lambda_B = \lambda_B\left[(\alpha_t + \xi_t)\cdot\Delta T + (1-p_e)\,\epsilon\right] \tag{3.9}$$

If we go deeper in the details we can write Eq. 3.9 as

$$\Delta\lambda_B = \lambda_B\left[\left(\alpha_t(T) + \frac{1}{n_{eff}(T)}\frac{dn_{eff}(T)}{dT}\right)\Delta T + \left(1 - \frac{n_{eff}^2(T)}{2}[\rho_{12} - \nu_P(T)(\rho_{11}-\rho_{12})\right)\epsilon\right] \tag{3.10}$$

if the strain is kept constant or

$$\Delta\lambda_B = \lambda_B\left[\left(\alpha_t(T) + \frac{1}{n_{eff}(T)}\frac{dn_{eff}(T)}{dT}\right)\Delta T + \left(1 - \frac{n_{eff}^2(T)}{2}[\rho_{12} - \nu_P(T)(\rho_{11}-\rho_{12})\right)\frac{\sigma}{E(T)}\right] \tag{3.11}$$

if it is the stress that is kept constant.

3.2 Experimental setup

In the experiments exposed in this chapter we used CCGs manufactured in $F\text{-}GeO_2$ doped silica fibers [24]. Typical grating lengths were $\sim 1mm$, or shorter, enabling beam characterization and temperature measurements with high spatial resolution.
Combining CCGs with a high speed and high resolution optical spectrum analyzer (Fig. 2.2), the fiber temperature (unstrained fiber), as well as fiber elongation (strained fiber), can be measured during CO_2-laser irradiation with equation 3.9.

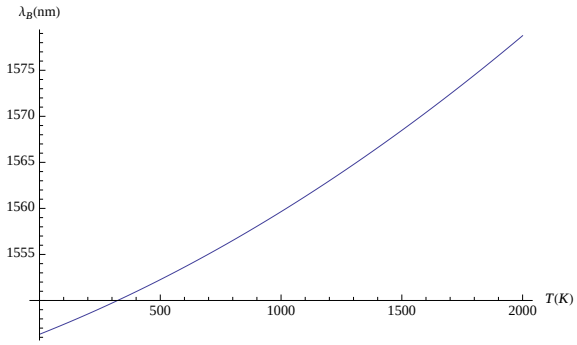

Figure 3.1: Calibration curve for temperature sensing realized on the data collected by Patrik Holmberg.

The calibrated thermal response of the CCG was measured by Patrik Holmberg [1] and was $\lambda_B = 1546.33 + 0.0104137T + 2.9 \cdot 10^{-6}T^2$ and it is shown in Fig. 3.1.
The strain response was measured to be $\Delta\lambda_B = 1.2pm/\mu\epsilon$.

3.3 Results

3.3.1 Experiment I [temperature profile]

A first experiment was to scan the beam transversally at a determined distance from the focus to characterize the beam temperature profile (Fig. 3.2). This time we used the plano-convex lens ($f = 5cm$) so to get to higher temperature and smaller beam waist. Doing so we can characterize the beam radius and the beam temperature at a determinate CO_2 laser power.

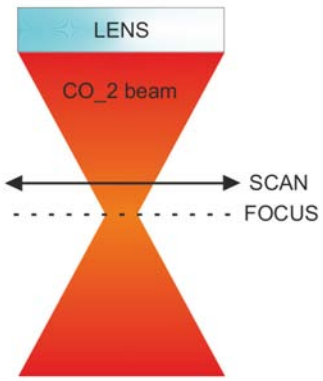

Figure 3.2: Scheme of the scan path through the beam in Experiment I.

In Fig. 3.3 we see the Bragg wavelength shift at different CO_2 output power while scanning perpendicularly to the beam. By converting the wavelength shift to the fiber temperature through the calibration curve we can reconstruct the temperature profile of the laser beam.

[1] PhD student at the Applied Physics Department, KTH (Laser Physics Group)

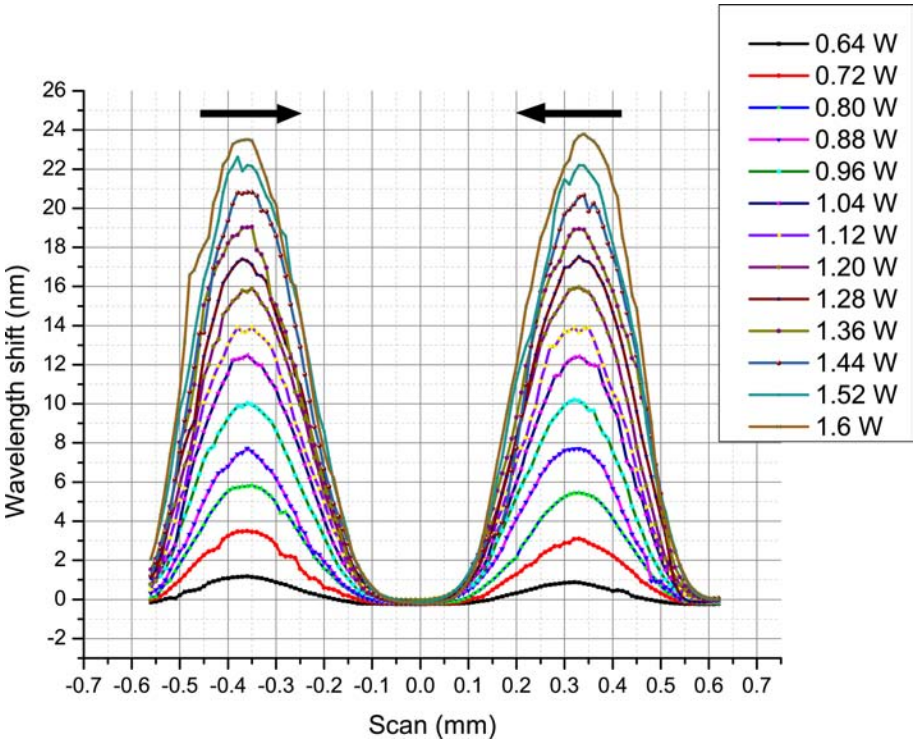

Figure 3.3: Experiment I: increasing temperature at fixed distance scanning temperature profile.

3.3.2 Experiment II [temperature profile]

After the first preliminary experiment we wanted to characterize the evolution of the beam radius and the temperature profile with the distance from the focus.
The second experiment was aimed also at measure the power absorbed by the fiber. By looking at a power meter positioned beyond the fiber (Fig. 4.4) and cross verifying it with the temperature rise of the fiber itself we can link the temperature rise to the power absorbed.
The fiber was fixed and it was hanging vertically while the laser was scanning the x axis. We then moved the fiber 2mm away from the lens and restarted the scanning of the laser (Fig. 3.4). We repeated this algorithm until the beam profile was complete.

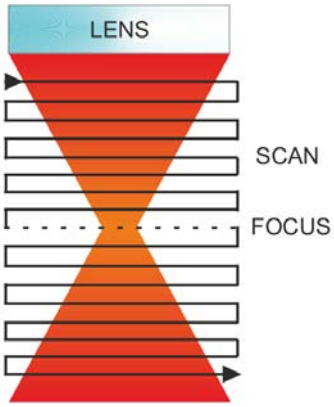

Figure 3.4: Scheme of the scan path through the beam in Experiment II.

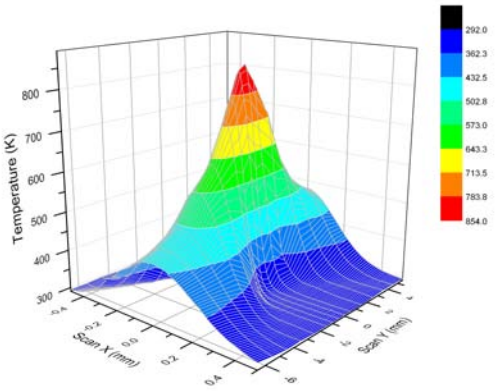

Figure 3.5: Experiment II: 3D laser beam temperature profile.

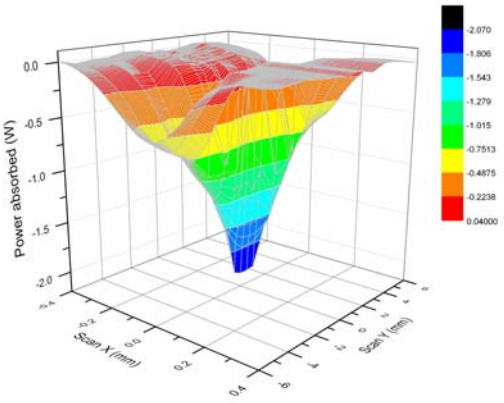

Figure 3.6: Experiment II: 3D laser beam power absorption.

A 2D contour plot is the perfect way to visualize the beam spatial profile combined with the temperature profile. We believe that the small asymmetry we find in Fig. 3.7 depends on the thermal inertia and is due to the scan path of the probe. In fact we made back and forth trips separated by pauses of a minute starting from the right side of the setup.

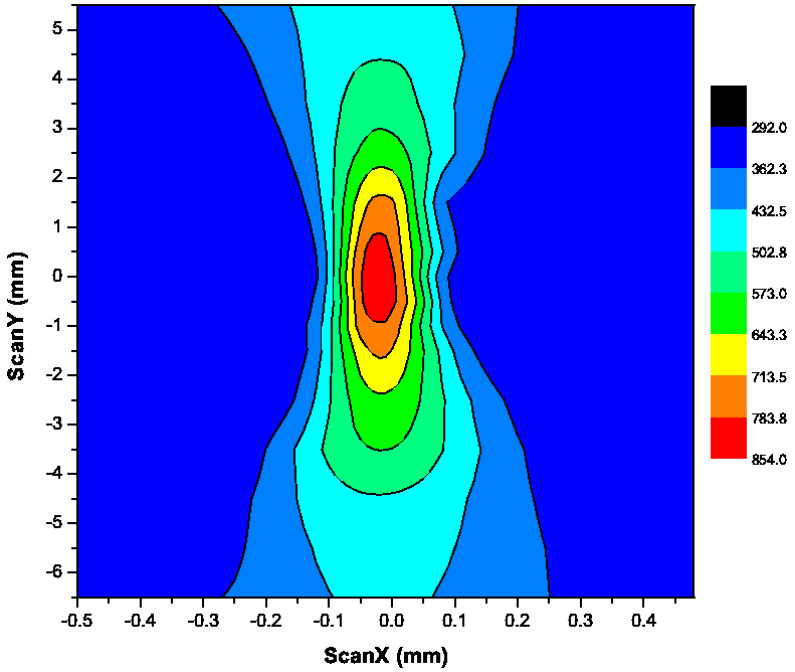

Figure 3.7: Experiment II: 2D-coloured temperature profile of the laser beam

3.3.3 Experiment III [heat capacity]

A third experiment was based on centring the laser on the fiber and then moving the fiber along the beam propagation direction (Fig. 3.8).
By looking at the temperature rise and at the power absorbed, with the laser beam perfectly centred on the fiber, we can analyse the heat capacity of silica fiber with temperature.

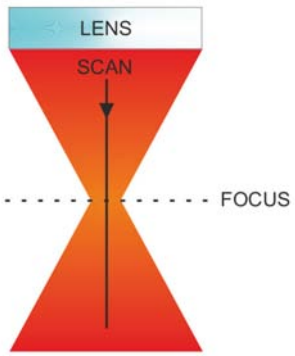

Figure 3.8: Scheme of the scan path through the beam in Experiment III.

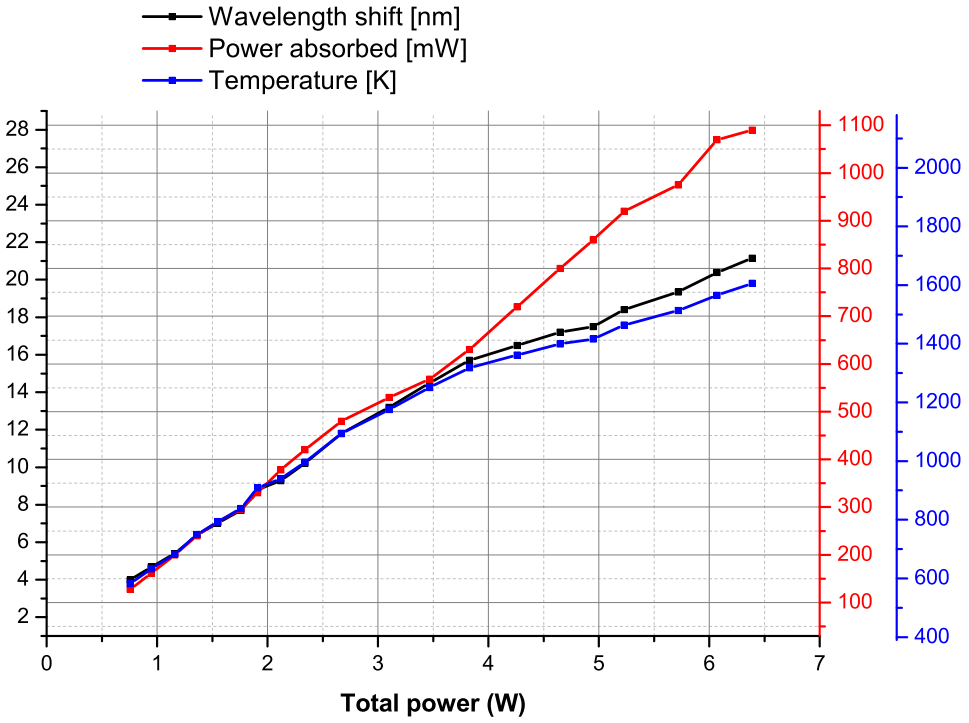

Figure 3.9: Experiment III: temperature variation with total power and power absorbed by the fiber.

3.4 Discussion

3.4.1 Temperature beam profile

With the first two experiments presented in the *Results* section we extensively characterized the temperature profile of the CO_2 laser beam.

Analysing Fig. 3.7 we obtain a beam waist of $\approx 110\mu m$ and a nearly symmetrical beam profile along the propagation direction, disturbed only by the thermal inertia of the fiber sensor.

Nevertheless, the results obtained from these experiments are of great relevance for the improvement of the process control to fabricate chiral gratings.

3.4.2 Heat capacity

There is not a consistent literature about silica fiber heat capacity at high temperature because it is difficult to measure heat capacity at so high temperatures.

The heat capacity C is the amount of heat required to change the temperature of a substance by a given amount ($[C] = J/K$).

The heat transfer from CO_2 to silica fiber depends strongly on the polarization of the laser beam.

$$\bar{R}_p = \int_0^{\pi/2} R_p \cos\theta \, d\theta = \int_0^{\pi/2} \left(\frac{-n\cos\theta + \sqrt{1 - \left(\frac{1}{n}\sin\theta\right)^2}}{n\cos\theta + \sqrt{1 - \left(\frac{1}{n}\sin\theta\right)^2}} \right)^2 \cos\theta \, d\theta \tag{3.12}$$

$$\bar{R}_s = \int_0^{\pi/2} R_s \cos\theta \, d\theta = \int_0^{\pi/2} \left(\frac{\cos\theta + \sqrt{n^2 - \sin^2\theta}}{\cos\theta + \sqrt{n^2 - \sin^2\theta}} \right)^2 \cos\theta \, d\theta \tag{3.13}$$

The power reflected is 9.5 % for p-polarized and 24 % for s-polarized.

In the literature the specific heat capacity of silica glass at room temperature is $703 J/Kg * K$ and the density of silicon dioxide at room temperature is $2196 kg/m^3$.

So we can easily obtain the volumetric heat capacity of silica, which is $1,54 J/cm^3 K$.

The volume of fiber heated was $\pi r^2 l = 7.85 * 10^{-11} m^3$ where $r_{fiber} = 62.5\mu m$ and $l = 6.4mm$.

The temperature rise time, which we defined as the time taken by the core of an SMF28 optical fiber to reach the steady state, was obtained by Patrik Holmberg and its value was stated as $0.45s$.

C_p is calculated by

$$C_p = \frac{\Delta P[W] \cdot t_{rise}[s]}{V[m^3] \cdot \Delta T[K]} \tag{3.14}$$

For example we can analyse the data obtained from Fig. 3.9. We have for each temperature the power absorbed and the total power of the laser. To get the variation of temperature x_n with absorbed power we can average between x_{n+2} and x_{n-1}

$T[K]$	$\Delta T[K]$	$\Delta Q[mW]$	$C_p[J/cm^3/K]$
666.2	167.9	56.0	1.91
712.9	161.0	54.5	1.93
760.1	155.4	47.5	1.78
829.5	158.8	45.0	1.62
866.3	145.9	54.0	2.12
917.2	158.9	62.5	2.25
1001.3	184.9	75.0	2.35
1057.7	236.9	76.0	1.84
1123.6	254.0	74.0	1.67
1205.8	224.0	75.0	1.92
1268.9	185.7	95.0	2.92
1325.2	149.2	116.0	4.46
1366.9	98.1	115.0	6.70
1412.8	102.1	100.0	5.61
1456.5	113.5	87.5	4.41
1490.4	149	105.0	4.04
1534.8	141.9	85.0	3.44

In Fig. 3.10 we represented the data from our experiment and compared it with the data available in the literature. More precisely data of the Heraeus quartz glass and from the site *www.efunda.com* are shown. These data are available only in a medium-low range of temperature, whereas we don't have any data above the transition temperature in the literature.
In our data we can clearly note a step around the **Transition Temperature**, which agrees with the theory and validate the preliminary study of this new method of measurement.

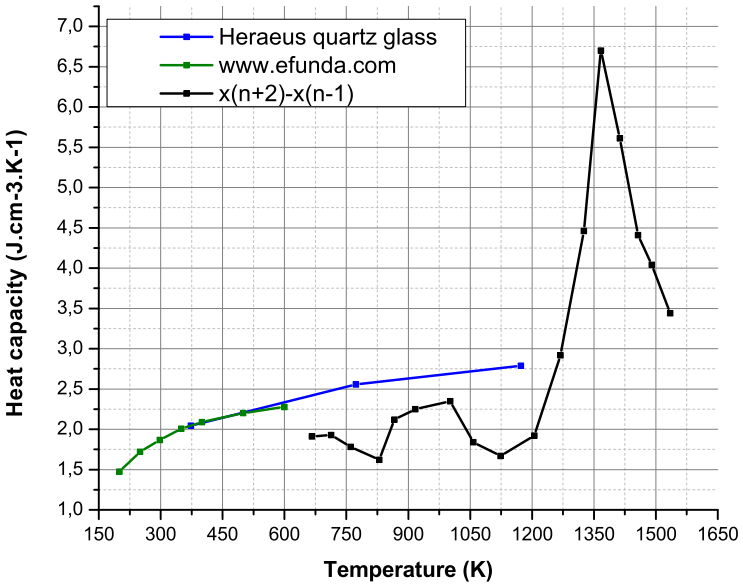

Figure 3.10: Heat capacity of fused silica [4] and calculated values from the performed experiments using a standard single mode fiber (SMF-28).

To improve our analysis we need to keep into account more information, like the polarization of the beam and the thermal history of the FBG.
If we improve this method, it could become a new and more precise method to measure heat capacity and its evolution with temperature within the glass transition region.

Chapter 4

Viscosity characterization

4.1 The temperature dependence

Before going through the discussion on viscosity characterization we need to understand what is viscosity and why it is so important in glass processing.
If we apply a shear force, atoms and molecular groups displace to each other. Viscosity is a measure of the resistance to shear deformation with time.
We will analyse viscosity through Newton's law:

$$\sigma = \eta\dot{e} \tag{4.1}$$

A great explanation of the physical processes underlying viscosity is found in [32] using Eyring's approach.
Viscosity depends greatly on temperature. This dependence can be explained by an Arrhenius rate-type equation:

$$\eta = \eta_0 exp\left(\Delta H/RT\right), \tag{4.2}$$

where R is the gas constant, η_0 is a pre-exponential factor, and ΔH is the activation energy for viscosity.
This would imply that a plot of $\ln\eta$ or $\log\eta$ vs. $1/T$ would be a straight line, the slope of which gives $\Delta H/R$.
The unit of measurement we will use throughout this thesis will be the $Pa \cdot s$.

4.2 Basics of viscosity measurements

The following four viscosity values are of great interest for engineering purpose [33] showed in Fig. 4.1

	$[\eta] = Pa \cdot s$	physical property
Working point	10^3	is delivered to the machine to be worked on
Softening point	$10^{6.65}$	can stand on his own
Annealing point	10^{12}	release 95% of its stresses within 15 minutes
Strain point	$10^{13.5}$	release its stresses over six hours

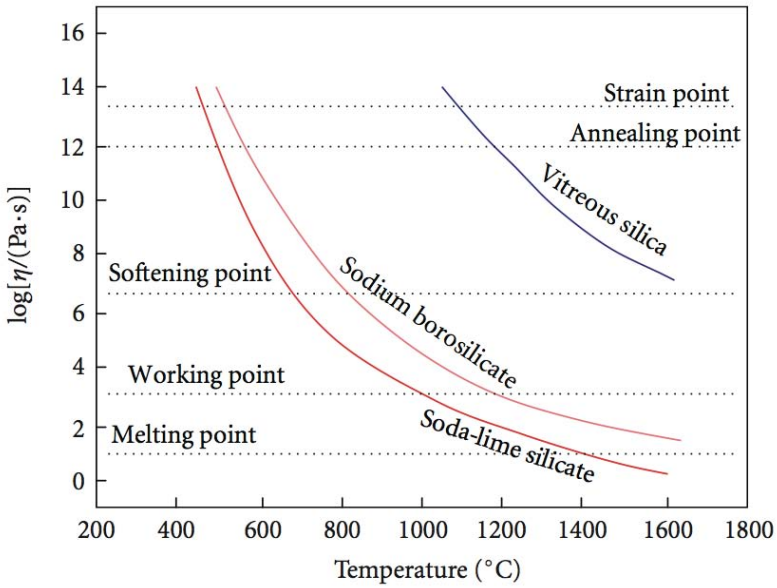

Figure 4.1: Viscosity points and viscosity curves of the main glasses [5].

We are interested in measuring viscosity in a fairly wide range around the softening point. Several techniques are available for this range [34]:

Method	$\log(\eta/Pa \cdot s)$
Parallel plate	$5 \div 9$
Penetration viscosimeter	$5 \div 9$
Fiber elongation	$5 \div 15.5$
Beam bending	$7 \div 12$
Disappearance of stress	$11 \div 14$

In this work we present a modified method based on the fiber elongation one. We will firstly explain the classic method for viscosity measurements.

Fiber elongation method

The fiber elongation viscometry is based upon the Littleton softening point determination.
I will synthesize the process described in ASTM C338 [35] and ISO 7884-3 [36].
The glass fiber must have a 0.55 to 0.75 mm diameter and be 235 mm long.
Before cutting the fiber one end is fused to make a ball.
The fiber is suspended inside a furnace, heated at a rate of $5K/min$, which covers only the top 10 cm [37].
We monitor the fall of the lower end of the fiber. The softening point corresponds to a rate of extension of $1mm/min$.
Attaching weights to the lower end we can raise the value of the higher measurable viscosity to$\log(\eta/Pa \cdot s) = 15$.

4.2.1 Modified fiber elongation technique

In this chapter we present a modification of the classic fiber elongation method to characterize the viscosity in an optical fiber.
The main requirements are the possibility to write an FBG into the fiber that needs to be characterized and the thermal stability of the aforementioned grating at relevant temperatures.
If we keep a fiber under strain and we heat it at sufficiently high temperature, it will permanently deform as $\sigma = \eta\dot{\epsilon}$. We can further develop the equation, and made it suitable for a linear strain:

$$\frac{F}{3 \cdot A} = \eta\dot{\epsilon} \tag{4.3}$$

where $\dot{\epsilon} = \Delta L/L$ is the elongation and A the area of a section of the optical fiber.
The elongation of a fiber containing a CCG will cause the grating pitch (Λ_B) to increase with a subsequent change in reflected Bragg wavelength ($\Delta\lambda_B$). As there is a direct relationship between ΔL, $\Delta\Lambda_B$ and $\Delta\lambda_B$, the equation used for determining viscosity by the fiber elongation method can be rewritten as

$$\eta = \frac{F}{3 \cdot \pi r^2} \cdot \frac{L}{\frac{dL}{dt}} \rightarrow \eta = \frac{F}{3 \cdot \pi r^2} \cdot \frac{\lambda_B}{\frac{d\lambda_B}{dt}} \tag{4.4}$$

Furthermore, if we take into account the temperature dependence of the Young modulus and we keep the strain constant $\sigma = F/S = E(T) \cdot \epsilon$ we can write Eq. 4.4 as

$$\eta = \frac{E(T) \cdot \epsilon}{3} \cdot \frac{L}{\frac{dL}{dt}} \rightarrow \eta = \frac{E(T) \cdot \epsilon}{3} \cdot \frac{\lambda_B}{\frac{d\lambda_B}{dt}} \tag{4.5}$$

The change in length measured by this method corresponds to the change in grating pitch ($\Lambda_B \sim 0.5\mu m$) averaged over a large number of periods. To investigate dynamic viscosity within the temperature interval 1000 to $2000K$ we developed two similar methods which see the phenomena at different scales.

FBG-based method

The FBG-based method (Fig. 4.2) analyses indirectly the change in length in the whole fiber between the two holder, in fact we do not irradiate directly the FBG.

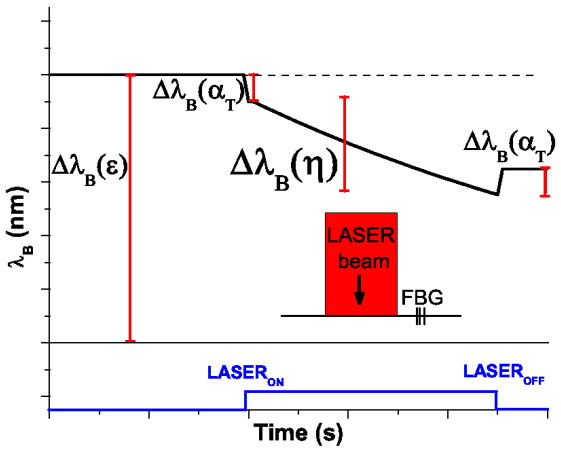

Figure 4.2: Method based on FBGs which monitor strain release due to fiber elongation.

We can now analyse each contribute to the wavelength shift throughout the whole experiment.
The wavelength shift $\Delta\lambda_B(\epsilon)$ is due to the strain applied to the fiber before irradiating it with the CO_2 laser beam.

We do this procedure so to enable and identify the release of stress due to viscosity decreasing at high temperatures.
Almost instantaneously ($\sim 0.45s$) after irradiating the fiber with the CO_2 laser beam the fiber expands because of the thermal expansion and the reflected Bragg wavelength shifts by $\Delta\lambda_B(\alpha_T)$ depending on the thermal expansion coefficient of the material and on the effective temperature of the heated fiber.
From this measurement we can indirectly (the FBG is not directly irradiated) obtain the value of the average temperature of the heated region ($\epsilon = \alpha_T \cdot \Delta T$).
The wavelength shift on which we must focus for the viscosity determination is $\Delta\lambda_B(\eta)$ and depends on the viscosity itself.
By averaging Eq. 4.5 we obtain

$$\Delta\lambda_B = \frac{E(T)\cdot\epsilon}{3}\cdot\frac{\lambda_B}{\eta}\Delta t \tag{4.6}$$

where Δt is the time of irradiation. We need to take into account that the change in wavelength for the FBG-method is indirectly related to the viscosity in the heated region, so

$$\Delta\lambda_B(\eta, FBG) = \Delta\lambda_B(\eta)\cdot\frac{L_{total}}{L_{heated}} \tag{4.7}$$

where L_{total} is the length of the fiber between the two holders and L_{heated} is the length of region heated by the almost flat top of the Gaussian CO_2 laser beam. Therefore, in our experiments the effective $\Delta\lambda_B$ is about ten times bigger than the measured one.
The shift due to thermal expansion is compensated by the shift due to thermal compression after the CO_2 laser beam is shut down. Therefore, we can obtain $\Delta\lambda_B(\eta)$ by simply calculating shift $\Delta\lambda_B$ before and after the irradiation.

CCG-base method

The CCG-based method (Fig. 4.3) analyses directly the change in length of the CCG grating.

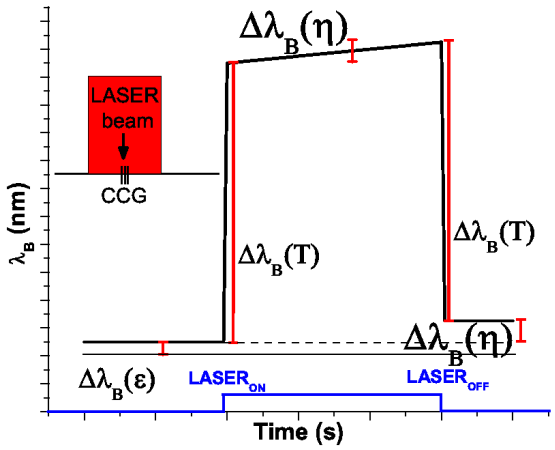

Figure 4.3: Method based on CCGs which directly probe fiber elongation.

This method is similar to the FBG-based one but should be far more precise, in fact the region of interest is no more the whole length of the fiber between the two holder but just the heated region, which, in our experiments, was approximately 1/10 of the length (which implies ten times the elongation or ten times the Bragg wavelength shift).
The key factor determining the effectiveness of the method is the thermal stability of CCGs at high temperatures. CCGs are in fact directly irradiated by the CO_2 laser beam and they need to withstand temperature well above $1000K$.
As for the FBG-based method the equation of reference is Eq. 4.6.

The novelty of this method lies in the order of magnitude of the length measured. We measure the evolution of Λ so, instead of tens of cm's (requiring advanced and tricky heating arrangements) we analyse changes in less than $1\mu m$ of fiber with a resolution of $1pm$. This is the reason we can measure the viscosity of silica fibers by heating them with a CO_2 laser. The data on the temperature profile of the CO_2 laser will will help us to improve the precision of the viscosity characterization.

4.3 Experimental setup

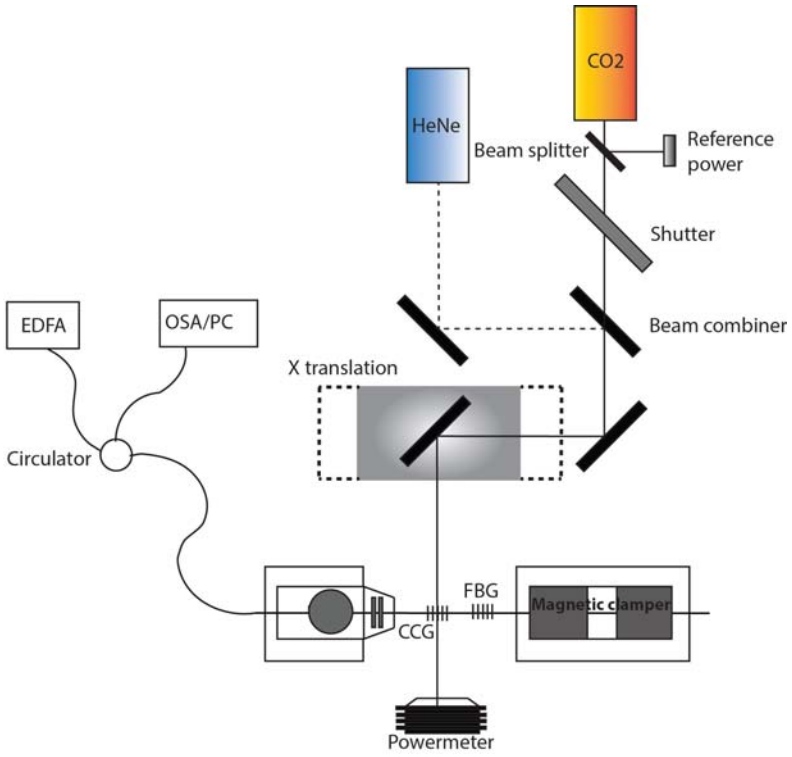

Figure 4.4: Experimental setup for the modified method to characterize viscosity

The CO_2-laser (ULR-25, $\mathrm{l} = 10.6\ \mu m$) had a maximum output power of $28W$ with a $1/e^2$-diameter of $\sim 6.5mm$. A HeNe laser was used as a visual guide. Thermal power meters where used as reference signal (1% tap) and to monitor the power absorbed by the fiber. The OSA (BaySpec FBGA-IRS) had a wavelength readout resolution of 1 pm and fast response time (up to 5kHz).
The length of the fiber between the two holders was $85mm$.
The holder worked for a maximum Bragg wavelength shift of $2 - 3nm$.
At a rate of $1.2pm/\mu\epsilon$ it corresponds to $2m\epsilon$ which stands for $170\mu m$ of fiber elongation.
We controlled the strain ϵ via our translation stage manually or by the piezo-controller and we double-checked it by calculation based on the strain-optic coefficient.
Following the methods procedures (Fig. 4.2 and Fig. 4.3), we measured the reflected Bragg wavelength λ_B and its evolution during a certain amount of time through the optical spectrum analyser (OSA).

4.4 Results

4.4.1 FBG-based measurements

We have then performed preliminary measurements based on the FBG based method explained in Fig. 4.2. We can clearly differentiate the contribution of the thermal expansion of the fiber and that of the visco-elastic behaviour of the glass. From the slope dominating the wavelength shift in the visco-elastic region we can extrapolate the viscosity at that particular temperature. Carrying out several experiments at different temperatures and strain (so that the time scale involved will be tailored to get the most from the experiment) allows us to plot the viscosity-temperature dependence.

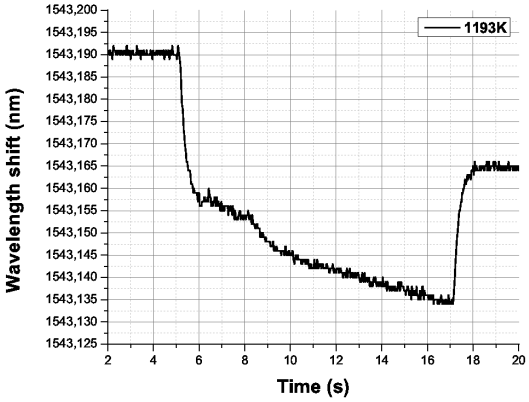

Figure 4.5: λ_B evolution under $1.5m$strain.

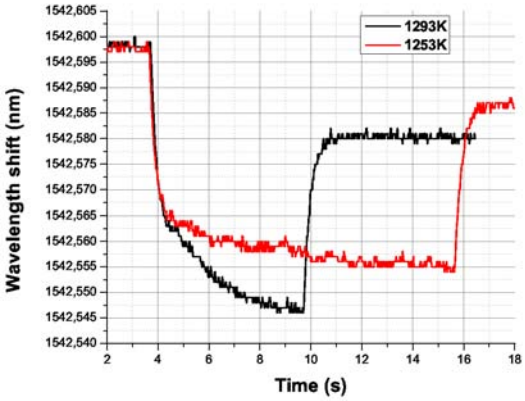

Figure 4.6: λ_B evolution under $1m$strain.

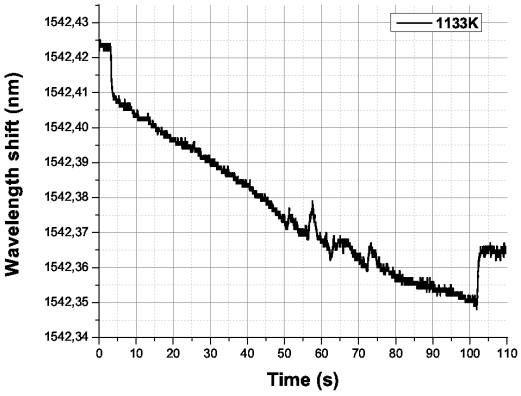

Figure 4.7: λ_B evolution under $1m$strain.

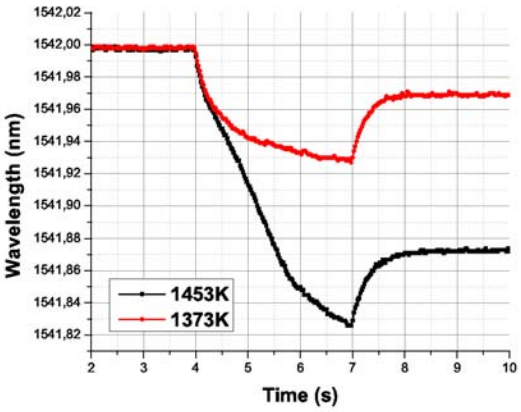

Figure 4.8: λ_B evolution under $0.5m$strain.

4.4.2 CCG-based measurements

We also performed preliminary measurements based on the CCG method explained in Fig. 4.3. The detailed image shows a clear reflected Bragg wavelength shift between the start and the end of the CO_2 irradiation.
The experiment that led to Fig. 4.11 was done by first heating the CCG without strain in order to see the stability of the grating and the possible impact of the irradiation on the reflected Bragg wavelength of the unstrained fiber. Then we strained the fiber until the reflected wavelength was equal to the starting wavelength of the previous step. Hence we carried on with the irradiation and wavelength shift measurements of the strained fiber. Once the data of the two experiments were collected we calculated the difference between the two final λ_B and used this value as the $\Delta\lambda_B(\eta)$ to further obtain the value of viscosity at that particular temperature.

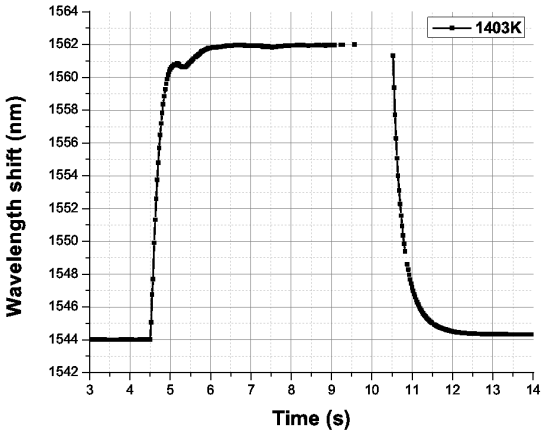

Figure 4.9: λ_B evolution under $0.6m$strain.

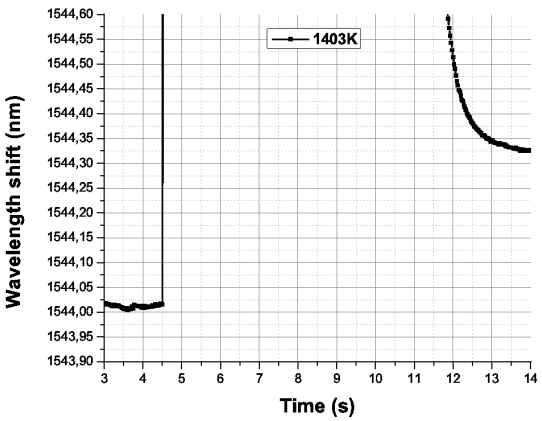

Figure 4.10: Detail of Fig. 4.9.

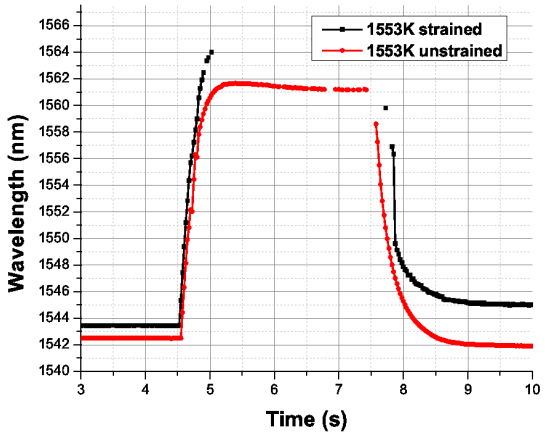

Figure 4.11: λ_B evolution under $1.2m$strain.

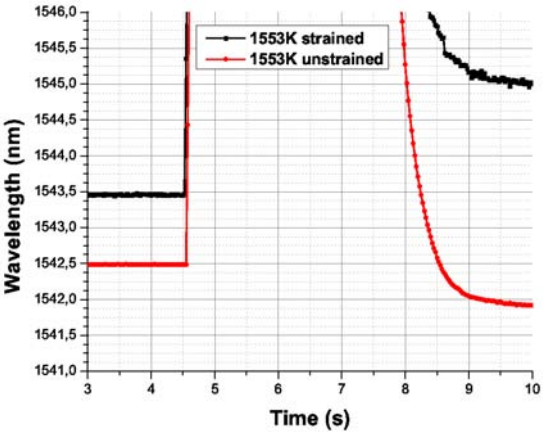

Figure 4.12: Detail of Fig. 4.11.

4.4.3 Viscosity data analysis

We can now analyse the raw data by means of Eq. 4.5
We know the Young modulus changes with temperature [38] and strain [39], which are the two key parameters of our interest.

$$E = 7.33 \cdot (1 + 1.365 \cdot 10^{-4} \cdot T) \cdot (1 + 5.75\epsilon) \cdot 10^9 \left[\frac{Kg}{m^3}\right] \tag{4.8}$$

with $273K \leq T \leq 1173K$. We then made the hypothesis that this equation is correct also above this temperature interval to have a qualitative idea of the behaviour at higher temperatures.
Analysing the raw results from the FBG-method and the CCG-method we obtain the following results and plot them in Fig. 4.15.

T [K]	$\lambda_B[nm]$	ϵ	E $[Kg/m^3]$	$\Delta\lambda_B[nm]$	$\Delta t[s]$	$\eta[Pa \cdot s]$
1133	1542.425	$1 \cdot 10^{-3}$	$8.512 \cdot 10^9$	0.060	100	$7.294 \cdot 10^{12}$
1193	1543.190	$1.5 \cdot 10^{-3}$	$8.597 \cdot 10^9$	0.025	12	$3.175 \cdot 10^{12}$
1253	1542.600	$0.5 \cdot 10^{-3}$	$8.633 \cdot 10^9$	0.011	12	$2.43 \cdot 10^{12}$
1293	1542.600	$0.5 \cdot 10^{-3}$	$8.673 \cdot 10^9$	0.018	6	$7.4 \cdot 10^{11}$
1373	1542.00	$0.5 \cdot 10^{-3}$	$8.729 \cdot 10^9$	0.030	3	$2.243 \cdot 10^{11}$
1453	1542.00	$0.5 \cdot 10^{-3}$	$8.809 \cdot 10^9$	0.130	3	$5.224 \cdot 10^{10}$

Figure 4.13: Data analysis from FBG-method raw data

T [K]	$\lambda_B[nm]$	ϵ	E $[Kg/m^3]$	$\Delta\lambda_B[nm]$	$\Delta t[s]$	$\eta[Pa \cdot s]$
1333	1543.800	$1.8 \cdot 10^{-3}$	$8.714 \cdot 10^9$	1.8	20	$1.270 \cdot 10^{12}$
1403	1544.000	$0.6 \cdot 10^{-3}$	$8.784 \cdot 10^9$	0.37	6	$8.406 \cdot 10^{11}$
1553	1543.500	$1.2 \cdot 10^{-3}$	$8.935 \cdot 10^9$	3.1	3	$7.56 \cdot 10^{10}$

Figure 4.14: Data analysis from CCG-method raw data

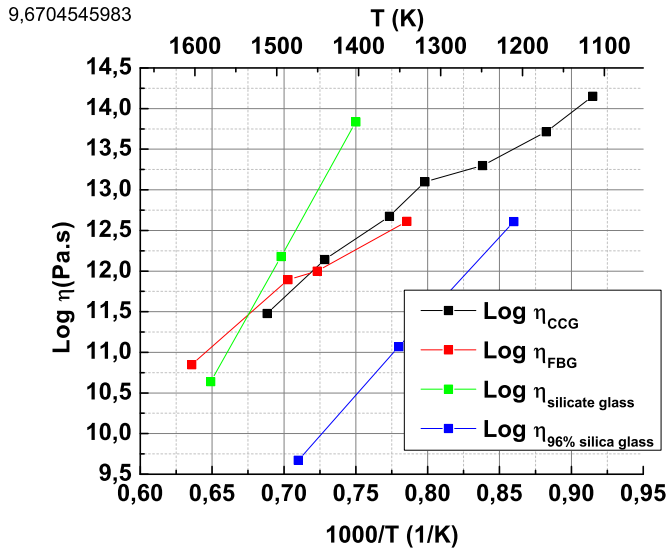

Figure 4.15: Viscosity data of silica glass and 96% of silica glass from literature [6] and calculated values from the performed experiments using a $F - GeO_2$ doped silica fiber.

4.5 Discussion

The lack of blank spots of data in all the six measurements obtained by the FBG-based method and the fairly good consistency of the results showed in Fig. 4.15 with the ones found in literature assure us on the reliability of the method.
A completely different discussion has to be made for the CCG-based method. Despite being the most promising method of the two, due to the higher sensibility, it requires a more sophisticated preparation. Developing a CCG is a time-consuming operation: we need to write an FBG and then it takes almost a day and a lot of carefulness to obtain a thermally stable sensor.
We produced only two reliable curves with this method, one of which has a lot of blank spots at $1553K$ (Fig. 4.11). Another curve was used for the preliminary viscosity calculation and it generated results of good consistency with the other experiments, but was not showed here because of the lack of sufficient data after the switching off of the CO_2 laser.
Nevertheless the results were very promising and we were able to outline also for the CCG-based method a clear trend in the viscosity-temperature behaviour (Fig. 4.15) consistent with literature data.
These are only preliminary results produced in a very short period of time and big uncertainties must be reduced in order to make this method more reliable and the results easily reproducible.

Chapter 5

Conclusions and outlook

The work presented in this thesis is mostly focused on the characterization of material properties of glass, aimed at understand and control the fabrication process of chiral fiber gratings.
A first aspect that is worth emphasizing is the possibility of a high temperature heat-capacity characterization of the fiber based on an integrated CCG sensor heated by a CO_2 laser beam. The literature lacks in data about this material property at high temperature due to difficulties in the measurements, which can be overcome by further develop our method based on direct temperature measurements of the fiber and absorption measurements by a power-meter placed behind the fiber itself.
We have verified through this method the step in heat-capacity at the glass transition temperature and it is in agreement with the same data obtained by our novel viscosity method (T_g is at $12Pa \cdot s$). Unfortunately the absolute values of the heat-capacity are a bit low and we need to refine the model.
The major achievement of this thesis concerns the characterization of the viscosity of a fiber. A novel method to measure the dynamic viscosity of optical fibers has been demonstrated, based on the ability of CCGs to accurately measure fiber temperatures as well as fiber elongation at elevated temperatures. By monitoring the grating wavelength of short gratings ($\sim 1mm$), localized inhomogeneous heating by CO_2-laser irradiation is made possible. The method therefore provides an advantage over traditional fiber elongation measurements, typically requiring flat temperature profile over tens of cm's.
We presented preliminary viscosity measurements of optical fibers, using the proposed method, for the temperature range 1000 to 2000K.
In these preliminary measurements we have used separately two sub-methods, one based on FBGs which monitor strain release due to fiber elongation and the other based on CCGs which directly probe fiber elongation and fiber temperature.
A suitable continuation in the development of the method will be to combine the two sub-methods in a single one, in order to be more accurate. We should then increase the limits of the temperature interval, which could be sensibly increased from the preliminary measurements.
If we control the viscosity and heat capacity of the fiber, the thermal and spatial profile of the CO_2 laser beam, we can also control the fabrication of CFGs, allowing the creation of a twisted fiber with non-collapsed micrometer holes with tailored pitch in the cladding.
This new kind of CFGs could also be suitable to study micro and nanofluidics.

Bibliography

[1] V. I. Kopp, V. M. Churikov, J. Singer, N. Chao, D. Neugroschl, and A. Z. Genack, "Chiral fiber gratings," *Science*, vol. 305, no. 5680, pp. 74–75, 2004.

[2] M. Sumetsky, D. J. DiGiovanni, Y. Dulashko, J. M. Fini, X. Liu, and et al., "Surface nanoscale axial photonics: robust fabrication of high-quality-factor microresonators," *Opt. Lett.*, vol. 36, no. 24, pp. 4824–4826, 2011.

[3] R. Kitamura, L. Pilon, and M. Jonasz, "Optical constants of silica glass from extreme ultraviolet to far infrared at near room temperature.," *Applied Optics*, vol. 46, no. 33, 2007.

[4] February 2013.

[5] W. D. Callister, *Fundamentals of Material Science and Engineering*. John Wiley and Sons, 2001.

[6] E. B. Shand, *Engineering Glass, Modern Materials*, vol. 6, p. 262. Academic Press, 1968.

[7] J. Langer, "The mysterious glass transition," *Physics today*, February 2007.

[8] A. K. Varshneya, *Fundamentals of Inorganic Glasses*, pp. 13–14. Academic Press, 1993.

[9] J. L. Garden, J. Richard, and H. Gillou, "Temperature of systems out of thermodynamic equilibrium," *J Chem Phys.*, September 2008.

[10] Pilkington, "Viscoelastic behaviour of glass and fictive temperature," pp. 2–4, 1998.

[11] G. W. Scherer, *Relaxation in glass and composites Relaxation in glass and composites Relaxation in glass and composites*. Wiley-Interscience, 1986.

[12] A. Q. Tool, "Viscosity and the extraordinary heat effects in glass," *J. Res.*, vol. 37, pp. 73–90, 1946.

[13] A. Q. Tool, "Relation between inelastic deformability and thermal expansion of glass in its annealing range," *J. Am. Ceram. Soc.*, vol. 29, pp. 240–53, 1946.

[14] A. Q. Tool, "Effect of heat-treatment on density and constitution of high-silica glasses of the borosilicate type," *J. Am. Ceram. Soc.*, vol. 31, no. 177-86, 1948.

[15] R. Kashyap, *Fiber Bragg Gratings*, p. 1. Academic Press, second ed., 2010.

[16] R. Kashyap, *Fiber Bragg Gratings*, p. 4. Academic Press, 2010.

[17] O. Svelto, "Fisica delle fibre ottiche," Marzo 2007.

[18] K. O. Hill, Y. Fujii, D. C. Johnson, and B. Kawasaki, "Photosensitivity in optical fibers waveguides: application to reflection filter fabrication," *Appl. Phys. Lett.*, vol. 32, pp. 647–9, 1978.

[19] G. Meltz, W. W. Morey, and W. H. Glenn, "Formation of bragg gratings in optical fibers by transverse holographic method," *Opt. Lett.*, vol. 32, no. 823-5, 1978.

[20] P. J. Lemaire, R. M. Atkins, V. Mizrahi, and W. A. Reed, "High pressure h2 loading as a technique for achieving ultrahigh sensitivity and thermal sensitivity in geo2 doped optical fibers," *Electronics Letters*, vol. 29, no. 13, pp. 1991–93, 1993.

[21] D. R. Paschotta, "Fiber bragg gratings."

[22] R. Ramaswami, K. N. Sivarajan, and G. H. Sasaki, *Optical networks: a practical perspective*. Elsevier, 2010.

[23] M. Fokine, *Photosensitivity, chemical composition gratings, and optical fiber based components*. PhD thesis, KTH, 2002.

[24] M. Fokine, "Thermal stability of chemical composition gratings in fluorine-germanium-doped silica fibers," *Optics Letters*, vol. 27, pp. 1016–1018, 2002.

[25] R. Kashyap, *Fiber Bragg Gratings*. Academic Press, second ed., 2010.

[26] R. Kashyap, *Fiber Bragg Gratings*, p. 58. Academic Press, 2010.

[27] V. I. Kopp, V. M. Churikov, G. Zhang, and et al., "Chiral fiber gratings: perspectives and challenges for sensing applications," in *Third European Workshop on Optical Fibre Sensors*, vol. 6619, July 2007.

[28] G. Adamovsky, S. F. Lyuksyutov, J. R. Mackey, and et al., "Peculiarities of thermo-optic coefficient under different temperature regimes in optical fibers containing fiber bragg gratings," *Optics Communications*, no. 285, pp. 766–773, 2012.

[29] S. Horinouchi, H. Imai, H. Yamasaki, and et al., "Second order nonlinear optical properties in silica-based glass film waveguides," *Journal of Nonlinear Optical Physics and Materials*, 1996.

[30] A. M. Prokhorov, *The Great Soviet Encyclopedia*. Macmillan, 1979.

[31] K. Rajogopal, *Engineering Physics*, p. 93. PHI, 2008.

[32] A. K. Varshneya, *Fundamentals of Inorganic Glasses*, pp. 183–185. Academic Press, 1993.

[33] A. K. Varshneya, *Fundamentals of Inorganic Glasses*, pp. 189–190. Academic Press, 1993.

[34] A. K. Varshneya, *Fundamentals of Inorganic Glasses*, p. 190. Academic Press, 1993.

[35] *ASTM C338-93: Standard Test Method for Softening Point of Glass.*

[36] *ISO 7884-3: Glass - Viscosity and viscometric fixed points, Part 3: "Determination of viscosity by fibre elongation viscometer"*, 1998-2002.

[37] A. K. Varshneya, *Fundamentals of Inorganic Glasses*, pp. 193–194. Academic Press, 1993.

[38] "Elastic moduli of glasses at elevated temperatures by a dynamic method," *Sam Spinner*.

[39] R. Brückner, "Properties and structure of vitreus silica," *Journal of non-crystalline solids*, vol. 5, p. 153, 1970.

Appendix A

VB programs

During this internship I made programs based on the event-driven programming paradigm aimed at automatically control the process of writing Fiber Bragg Gratings. The devices are controlled using the APT Active X and ddl libraries in the Visual Basic environment. I attach an example of a typical program to control the instruments (e.g., motors or shutters).

```
Imports System.Globalization
Imports System.IO
Imports System.Math

Public Class FBG_Basic

    Declare Function pl1000OpenUnit Lib "pl1000.dll" (ByRef handle As Short) As
        Integer
    Declare Function pl1000CloseUnit Lib "pl1000.dll" (ByVal handle As Short) As
        Integer
    Declare Function pl1000SetDo Lib "pl1000.dll" (ByVal handle As Short, ByVal
        do_value As Integer, ByVal doNo As Integer) As Integer
    Dim provider As New CultureInfo("en US") '("sv SE")
    Dim status As Short
    Dim HandlePL As Integer

    Private Sub Form1_Load(ByVal sender As System.Object, ByVal e As System.
        EventArgs)
    Handles MyBase.Load

        AxMG17Motor1.StartCtrl()
        MotorTranslationLeft.StartCtrl()
        MotorRotationLeft.StartCtrl()
        MotorTranslationRight.StartCtrl()
        MotorRotationRight.StartCtrl()

        status = pl1000OpenUnit(HandlePL)
        If HandlePL = 0 Then

            MsgBox("Unable to open PicoLog")
        End If
    End Sub

    Private Sub AxMG17Motor1_Enter(ByVal sender As System.Object, ByVal e As System
        .EventArgs) Handles AxMG17Motor1.Enter

    End Sub

    Sub OpenShutter()
        pl1000SetDo(HandlePL, 1, 0)

    End Sub

    Sub CloseShutter()
        pl1000SetDo(HandlePL, 0, 0)
```

```
End Sub

Private Sub AxMG17Motor2_Enter(ByVal sender As System.Object, ByVal e As System
    .EventArgs) Handles MotorTranslationLeft.Enter

End Sub

Private Sub myWaitFun(ByVal delay As Double)
    Dim watch As New Stopwatch
    Dim frequency As Double = Stopwatch.Frequency / 1000000

    'sysTimeStamp_ticks = Stopwatch.GetTimestamp ' returns time stamp in ticks
        before delay

    watch.Start()
    Do While watch.ElapsedTicks / frequency < delay
        Application.DoEvents()
    Loop
    watch.Stop()
End Sub

Private Sub ButtonHome_Click(ByVal sender As System.Object, ByVal e As System.
    EventArgs) Handles ButtonHome.Click
    MotorRotationLeft.MoveHome(0, False)
    MotorRotationRight.MoveHome(0, False)
    MotorTranslationLeft.MoveHome(0, False)
    MotorTranslationRight.MoveHome(0, False)
    AxMG17Motor1.MoveHome(0, False)
End Sub

Private Sub Button1_Click_1(ByVal sender As System.Object, ByVal e As System.
    EventArgs) Handles ShutterOpen.Click
    pl1000SetDo(HandlePL, 1, 0)
End Sub

Private Sub ShutterClose_Click(ByVal sender As System.Object, ByVal e As System
    .EventArgs) Handles ShutterClose.Click
    pl1000SetDo(HandlePL, 0, 0)
End Sub

Private Sub Label6_Click(ByVal sender As System.Object, ByVal e As System.
    EventArgs) Handles Label6.Click

End Sub

Private Sub GO_Click(ByVal sender As System.Object, ByVal e As System.EventArgs
    ) Handles GO.Click
    Dim acceleration As Single = Single.Parse(TextAcceleration.Text, provider)
    Dim speed As Single = Single.Parse(TextSpeed.Text, provider)
    Dim length As Integer = TextLength.Text()
    Dim shutterDelay As Single = Single.Parse(TextDelay.Text, provider)
    Dim startPos As Single = Single.Parse(TextStart.Text, provider)
    Dim pos As Single
    Dim posPart As Single = startPos
    Dim posFin As Single = startPos + length
    Dim flag As Integer = 0
    Dim flag2 As Integer = 0
    Dim flag3 As Integer = 0

    Call AxMG17Motor1.MoveHome(0, False)

    AxMG17Motor1.GetPosition(0, pos)

    While pos > 0.1
        AxMG17Motor1.GetPosition(0, pos)
    End While

    Delay(2)

    Call AxMG17Motor1.SetVelParams(0, 0, 0.2, 2)
```

```
        Call AxMG17Motor1.MoveRelativeEnc(0, posPart, 0, 1000, False)
        AxMG17Motor1.GetPosition(0, pos)

        While flag2 = 0
            If pos > posPart    0.1 Then
                Delay(shutterDelay)
                Call AxMG17Motor1.SetVelParams(0, 0, speed, acceleration)
                Call AxMG17Motor1.MoveRelativeEnc(0, length, 0, 1000, False)
                pl1000SetDo(HandlePL, 1, 0)
                flag2 = 1
            End If
            AxMG17Motor1.GetPosition(0, pos)
        End While

        AxMG17Motor1.GetPosition(0, pos)

        While flag3 = 0
            If pos > posFin    0.01 Then
                flag3 = 1
                pl1000SetDo(HandlePL, 0, 0)
            Else : AxMG17Motor1.GetPosition(0, pos)
            End If
        End While

    End Sub

    Sub Delay(ByVal dblSecs As Double)

        Const OneSec As Double = 1.0# / (1440.0# * 60.0#)
        Dim dblWaitTil As Date
        Now.AddSeconds(OneSec)
        dblWaitTil = Now.AddSeconds(OneSec).AddSeconds(dblSecs)
        Do Until Now > dblWaitTil
            Application.DoEvents() ' Allow windows messages to be processed
        Loop
    End Sub

End Class
```

Appendix B

Evaluation and purchase of tools

During my three months internship at KTH I have also dealt with the evaluation and purchase of tools needed to perform the experiments.
It was a matter of responsibility and planning skills due to the high value of the instruments and the bonds in time for the realization of the experiments.
Here I have made a list of the tools purchased for the experiments during my internship:

- SM1A36 - Adapter with External M27 x 0.5 Threads and Internal SM1 Threads (kr 181,31/ 21 Euro)
- NFL5DP20S/M - NanoFlex 5 mm Translation Stage with Diff. Drive and Feedback Piezo (kr 12.198,00/ 1420 Euro)
- PT1/M-Z8 - Single-Axis, 25 mm Travel, Motorized Translation Stage (kr 6.270,86/ 730 Euro)
- TPZ001 - T-Cube 150 V Piezo Driver (Power Supply Not Included) (kr 5.462,10/ 636 Euro)

The total amount of money used to buy new instruments was kr 24.112/ 2.807 Euro.